

# Enhanced Control and Power Management for a Renewable Energy-Based Water Pumping System

MAHMOUD A. MOSSA<sup>1</sup>, OLFA GAM<sup>2</sup>, NICOLA BIANCHI<sup>3</sup>, (Fellow, IEEE), AND NGUYEN VU QUYNH<sup>4</sup>

<sup>1</sup>Electrical Engineering Department, Faculty of Engineering, Minia University, Minia 61111, Egypt

<sup>2</sup>Département École de Génie, Université Québec en Abitibi Témiscamingue, Rouyn-Noranda, QC J9X 5E4, Canada

<sup>3</sup>Department of Industrial Engineering, University of Padova, 35131 Padova, Italy

<sup>4</sup>Electrical and Electronics Department, Lac Hong University, Bien Hoa, Dong Nai 810000, Vietnam

Corresponding authors: Mahmoud A. Mossa (mahmoud\_a\_mossa@mu.edu.eg) and Nguyen Vu Quynh (vuquynh@lhu.edu.vn)

This work was supported in part by the Cultural Affairs and Missions Sector at the Ministry of Higher Education in Egypt, and in part by the Lac Hong University in Vietnam.

**ABSTRACT** The paper introduces a comprehensive dynamic analysis for a renewable energy based water pumping system. The complete system components are described in details. The components include a wind turbine power system, a permanent magnet synchronous generator (PMSG), a water pumping system and a battery. The storage system is used to enhance the power delivery under weak wind production which consequently enhances the system reliability. Considering the PMSG as the fundamental power unit in the system, a new predictive control procedure is presented to enhance the PMSG performance. To validate the effectiveness of the proposed control scheme, a detailed comparison is accomplished between the designed controller and other three traditional controllers to evaluate the most effective in between. A power management scheme is constructed to manage the power flow and ensuring a sufficient power delivery to the pumping system. The obtained results are presented and analyzed in details to compare between the dynamics of the four predictive controllers used to manage the generator operation. The results report that the formulated control scheme has the best performance in terms of the reduced fluctuations, low calculation capacity, structure simplicity and low currents THD. The obtained results also approve the validness of the designed power management strategy in balancing the power flow and stabilizing the DC bus voltage as well.

**INDEX TERMS** PMSG, predictive control, power management, battery storage, water pumping system, voltage control.

## ACRONYMS AND SYMBOLS

<i>PC</i>	Predictive control	$\omega_g$	Rotor speed	<i>MSC</i>	Machine side converter	$u_{dg}, u_{qg}$	<i>d-q</i> voltages
<i>MPC</i>	Model predictive control	$\omega_s$	Rotor electrical speed	<i>CF</i>	Cost function	$U_{dc}, U_{dc}^*$	Real and command DC bus voltages
<i>DPC</i>	Direct power control	$p$	Pole pairs	<i>DOD</i>	Depth of discharge	$C$	Capacitor of DC bus
<i>WPS</i>	Water pumping system	$\psi_g$	PMSG flux	$S_f$	Weighting scale	$C_s, C_b$	Battery element capacitances
<i>CCS</i>	Continuous control set	$\psi_m$	Rotor flux	<i>MPI</i>	Motor-pump inverter	$R_s, R_e, R_t$	Battery element resistances
<i>FCS</i>	Finite control set	$i_{dg}, i_{qg}$	<i>d-q</i> currents	<i>IM</i>	Induction motor	$U_{bat}, U_{cb}, U_{cs}$	Bulk and surface capacitance voltages

The associate editor coordinating the review of this manuscript and approving it for publication was Akshay Kumar Saha<sup>1</sup>.

<i>HPS</i>	Hybrid power system	$I_{bat}, I_b, I_s$	Battery, bulk and surface currents	$F$	Friction coefficient	$T_s$	Sampling time
<i>BSS</i>	Battery storage system	$U_{m,bat}, I_{m,bat}$	Battery modulated voltage and current	$P_g, P_g^*$	Calculated and reference active powers	$K_{P,i_d}, K_{I,i_d}, K_{P,i_q}, K_{I,i_q}$	Coefficients of IM current controllers
<i>PSS</i>	Power sharing strategy	$m_{bat}$	Modulation index	$Q_g, Q_g^*$	Calculated and reference reactive powers	$K_{P,\omega_m}, K_{I,\omega_m}$	Coefficients of IM speed controller
<i>PMS</i>	Power management system	$R_p, R_s$	Primary and secondary resistances of IM	$P_{nom}, Q_{nom}$	Rated generator powers	$K_{P\psi}, K_{I\psi}$	Coefficients of PMSG flux controller
<i>UCS</i>	Units control stage	$L_{lp}, L_{ls}$	Primary and secondary leakage inductances	$T_{nom}, \psi_{nom}$	Rated generator torque and flux	$K_{PT}, K_{IT}$	Coefficients of PMSG torque controller
<i>SMU</i>	Switching management unit	$L_s, L_r, L_m$	Stator, rotor and mutual inductances of IM	$R$	Stator resistance	$K_{p,dc}, K_{i,dc}, K_{d,dc}$	Coefficients of DC bus PID controller
<i>SOC</i>	Battery state of charge	$\omega_m, \omega_{me}$	Mechanical and electrical rotor speeds of IM	$L_s$	Stator inductance	$K_{p,B}, K_{i,B}, K_{d,B}$	Coefficients of battery system PID controller
$\beta$	Blade pitch angle	$n_p$	Pole pairs number of IM	<b>I. INTRODUCTION</b>			
$\mu, \mu_{opt}$	Actual and optimal tip speed ratios	$\bar{u}_s^{rf}, \bar{\psi}_s^{rf}$ and $\bar{i}_s^{rf}$	Stator voltage, stator current and stator flux of IM defined in rotor flux rotating frame	The global warming and the depletion of natural energy sources urged the need to search for alternative solutions through utilizing the available renewable energy sources [1]–[3]. The sun, wind, geothermal and wave energies represent some forms of such renewable energy sources [4]. The renewable energy systems are considered as a promising solution to solve the electrification needs in the remote isolated areas [5], [6]. Among these types of renewable sources, the wind energy is paid great concern to electrify the isolated hilly areas in the forms of illuminating and water pumping for irrigation systems [7].			
$V_w$	Wind speed	$\bar{\psi}_r^{rf}$ and $\bar{i}_r^{rf}$	Rotor flux and rotor current defined in rotor flux rotating frame	In general, the wind energy suffers from the intermittent operation. To achieve the optimal wind power exploitation, smart controllers must be utilized to ensure the continuity of the generation and to provide proper steady state and transient operations as well [8]. To overcome the issue of wind discontinuity, a storage system is essentially incorporated to compensate the shortages due to wind gust and arbitrary load changes [9], [10]. However, managing the storage system besides controlling the main wind generation system is also a challenge, which must be handled properly to achieve a smooth power profile for the entire irrigation system. To fulfill these requirements, different contributions in the literature are presented. For example, in [11]–[13], the researchers shed the light on MPPT algorithms which are used to optimally exploit the power regardless of the weather parameters variation. Other studies concerned with the optimum sizing of different units of water pumping system to achieve the balance between the produced and consumed powers [14]–[16]. Other study has concerned with analyzing the relationship between the cost and system reliability [17]. The studies in [18]–[20], constructed efficient control systems to manage the operation			
$V_{w,nom}$	Nominal wind speed	$T_e, T_l$	Developed and load torques of IM				
$C_p$	Turbine power coefficient	$J_m$	IM moment of inertia				
$P_t$	Turbine power	$P_{pump}$	Pump power				
$P_w$	Wind power	$H$	Water height (m)				
$T_g, T_f, T_t$	Generator, friction and turbine torques.	$Q$	Water flow rate ( $m^3/s$ )				
$J_t, J_g$	Turbine and generator inertias, respectively.	$\Delta T$	Pump operation time (s)				

of power converters to achieve maximum power extraction. In [21]–[23], different types of PMS are adopted to optimally operate each energy unit inside the hybrid system. The main task of the PMS is to obtain the optimal reference power of each system unit, which finally results in settling the DC link voltage with minimum fluctuations.

The generator is considered as the main important part in the wind generation system, which feeds the water pump. Thus, designing an effective control system that guarantees the proper operation is indispensable. Different machine types are used as a generation unit. The squirrel cage induction generator is used initially with the capability of parallel running [24], [25]. However, the main drawback of this generator is the need of a separate source of reactive power (i.e. capacitor banks). Another used generator type is the slip-ring induction generator, known also as doubly fed induction generator (DFIG), which provided several advantages compared with the squirrel cage type [26], [27]. The DFIG enabled the application of control from two sides: the stator or rotor terminals. Controlling the DFIG from rotor side provided an advantage of using low power scale converters, which saved the cost. In addition, the DFIG possessed the fault tolerant capability, which is realized via considering a certain modification in the control algorithm. However, the maintenance cost of the DFIG is remarkable; this is in addition to the low efficiency due to the winding copper losses. The PMSG then came into consideration due to its multiple advantages [28], [29], such as the ability to operate at high efficiency, solid structure and ability to work without gear systems. For these reasons, the surface mounted PMSG is used in the current study as the main generation unit.

Designing an effective control system to manage the PMSG operation is a vital requirement. The control targets for the PMSG include limiting the power, torque and current ripples. Limiting the torque ripples is specifically a vital need to suppress the shaft vibrations, which may harm the mechanical coupling system. In addition, limiting the current harmonics is another need to ensure high power quality. Different control schemes are adopted to manage the dynamics of PMSG; at beginning, the field oriented control (FOC) is used [30], [31], in which an independent control of the active and reactive power or torque and flux is achieved through designing two separate inner current control loops. Sufficient steady state dynamic performance is achieved, however the response delay and system complexity were the most deficiencies of such technique. In order to avoid the FOC shortages, the direct torque control (DTC) is introduced and used with the PMSG [32], [33]. The DTC can be implemented without using a modulation scheme (i.e. PWM) as in FOC. In addition, it can be applied directly in the stator frame which prevents the utilization of co-ordinate transformations as adopted in FOC. All of these features simplified the structure of DTC. Furthermore, the DTC succeeded in achieving a faster dynamic response compared with the FOC. Nonetheless, the main deficiency of the DTC was the high ripples and variable switching frequency because of the used hysteresis

comparators. Another scheme which adopts a similar operation principle to the DTC is the direct power control (DPC) [34]–[36]. The DPC is a transpose of the DTC, which replaces the torque and flux control in DTC with active and reactive powers control, respectively. The DPC uses external control loops for the powers, which are evaluated directly from the measured voltages and currents. This made the DPC more robust than the DTC which depended on the model parameters to evaluate the torque and flux. To avoid the shortages in the FOC, DTC and DPC as well, different modern controllers are presented such as fuzzy control (FC) [37], sliding mode control (SMC) [38] and predictive control (PC) [39], [40]. Among these controllers, the PC has succeeded in bringing the researchers' interest due to its several advantages such as: simple structure, flexibility, ability to handle different system nonlinearities, ability to work without modulation stages and achieving different control targets at the same time.

Consequently, the PC theory is used to overcome the drawbacks of FOC, DTC and DPC via excluding the PI current controllers in FOC, and hysteresis comparators in DTC and DPC with only one simple cost function (CF), which is used to generate the reference signals after accomplishing an optimization process. After generating the reference signals using the CF, there are two possible ways to handle the references to the controlled item (i.e. the generator); one through using a continuous control set (CCS) PC which considers the average model of the converters and using a PWM [41], [42], and the other via considering the finite control set (FCS) PC which considers the discrete converter model and selects from definite possible vectors without using a PWM [42], [43]. Due to its simplicity, the FCS is used in our study to provide the reference signals to the PMSG terminals.

Thus, via applying the PC principle, the classic DTC and DPC are replaced with the model predictive DTC (MP DTC), and model predictive DPC (MP DPC), respectively. In the MP DTC, a CF incorporates the normalized flux and torque errors is utilized. This is in addition to using a scaling factor ( $S_f$ ) that is used to balance the importance of flux control respecting to the torque control [44]. In the same manner, the MP DPC utilizes a CF which combines the standardized power errors besides using a weighting scale [45]. The MP DTC and MP DPC have succeeded in solving the problems of DTC and DPC, respectively via reducing the ripples content while maintaining the switching frequency within the permissible ranges. However, the ripples are still present and not completely eliminated; in addition, the high computation burden of the two predictive controllers is still a challenge. Furthermore, using a weighting scale  $S_f$  in the MP DPC and MP DTC can affect the control if it is not appropriately identified. Attempts are made to avoid the wrong selection of  $S_f$  through adopting online adaptation schemes [46], [47]. Good results are obtained using the optimally selected  $S_f$ ; however the computation burden is further increased. Other control topologies turned their direction towards the elimination of  $S_f$  from the CF such as model predictive current control (MP CC), which uses a CF consists of two comparable items (the

errors of the  $d$ - $q$  currents). Sufficient performance is obtained with the MP CC [48], however the computation burden is still remarkable due to the dependency on the model parameters.

The ripples in the MP DPC, MP DTC and MP CC schemes can be inferred to many reasons; one of these reasons is the utilization of only one voltage vector during the execution cycle, and it is possible that the absolute error of one variable deviates and causes the ripple increase. To solve this issue, different studies considered multiple vectors in the same sampling interval [49], [50]. This helped effectively in suppressing the ripples, but the system complexity and consequently the computation capacity are inversely affected. Thus, formulating a CF without scale factor and using simple terms to save the computation regime is a vital need. To fulfill these requirements, the current study proposed a predictive voltage control (PVC) scheme which utilizes a CF deals with the voltage signals deviation. The actual voltage terms are obtained using the FCS principle; meanwhile the reference voltage terms are obtained using two designed PI regulators. Thus, the PVC does not utilize any estimated variables or a weighting scale, which saves the computation, and make the controller more robust. A comparison is carried out between the performances of PMSG using the the proposed predictive scheme and other three known predictive schemes to approve the superiority of the designed control algorithm.

Furthermore, the present study provides the design of an effective power management strategy to secure the power equilibrium between the different system units (Wind driven PMSG, battery storage unit, and water pumping system).

The presented study contributes to the literature by the following items

- The paper presents a comprehensive description of a hybrid power system (HPS) utilized for water pumping applications in remote areas.
- The design and modeling of all system parts are explained in details.
- An efficient power management strategy (PMS) is developed to balance the power flow in the hybrid system.
- A new PVC control scheme is presented to enhance the PMSG dynamics.
- A comprehensive comparison and performance analysis is accomplished between the proposed PVC and other three predictive schemes used previously with the PMSG.
- The formulated PVC showed high performance in comparison with the other predictive controllers overcoming the previous deficiencies and enhancing the PMSG dynamics.
- The present study can be considered as a base for future work in which additional energy sources (i.e. wave, fuelcell, solar) can be incorporated in favour of studying the system reliability.

The present study is arranged as: in Sec. II, the wind system including the PMSG is presented and described in details. In Sec. III, the battery model, the converter model

and motor-pump unit model are presented and described in details. In Sec. IV, the supervisory hierarchical management system for the entire units is introduced and described in details. In Sec. V, the control of each system unit is presented. Sec. VI presents the test results and analyzes it. Finally, Sec. VII presents the conclusions of the study.

## II. MODELING OF WIND TURBINE AND GENERATOR SYSTEM

### A. MODELING OF WIND TURBINE

The system model of the wind turbine must be constructed precisely in order to emulate the wind speed variation. The model should incorporates the pitch angle ( $\beta$ ) and MPPT control units. The MPPT is used to optimally exploit the wind power for the normal wind speed operation; this is realized via utilizing the optimal ratio ( $\mu_{opt}$ ) [51]. On the other hand, the pitch control is applied to restrict the power when the wind speed is higher than the rated. The pitch control identifies a specific pitch angle for each wind speed ( $V_w$ ) variation with the help of a pitch servo system which utilizes a recorded  $V_w$ - $\beta$  curve. The ratio  $\mu$  is defined by

$$\mu = \frac{r\omega_t}{V_w} \quad (1)$$

where  $r$  is the blade radius.

The turbine power coefficient  $C_p$  is given by

$$C_p(\mu, \beta) = 0.53 \left[ \frac{151}{\mu_i} - 0.58\beta - 0.002\beta^{2.14} - 13.2 \right] \times e^{\left(\frac{-18.4}{\mu_i}\right)} \quad (2)$$

where  $\mu_i = \frac{1}{\frac{1}{\mu - 0.02\beta} - \frac{0.003}{\beta^{3+1}}}$ .

The wind and turbine powers are evaluated by

$$P_w = \frac{1}{2} \rho A V_w^3 \quad \text{and} \quad P_t = C_p P_w \quad (3)$$

where  $A$  is the swept area, and  $\rho$  is the density of the air.

Using (1), (2) and (3), the shaft torque is given by

$$T_t = \frac{P_t}{\omega_t} = \frac{C_p \cdot \frac{1}{2} \rho A V_w^3}{\omega_t} \quad (4)$$

The generator torque and speed are obtained by

$$\begin{aligned} T_g &= \frac{T_t}{G} \\ \omega_g &= G\omega_t \end{aligned} \quad (5)$$

Furthermore, the turbine shaft dynamics is expressed by

$$T_t - GT_g - FG\omega_t = \left( \frac{J_t}{G} + GJ_g \right) \frac{d\omega_t}{dt} \quad (7)$$

To activate the MPPT mode, an optimal value ( $\mu_{opt}$ ) is imposed.

Using these presumptions, the speeds reference signals to be utilized can be defined by

$$\omega_t^* = \frac{\mu_{opt} V_w}{R} \quad (8)$$

$$\omega_g^* = G\omega_t^* \quad (9)$$

**B. MODELING OF PMSG**

The model of the PMSG can be represented discretely at instant  $kT_s$  by

$$\frac{di_{dg,k}}{dt} = \frac{1}{L_s} (u_{dg,k} - Ri_{dg,k} + \omega_{s,k}L_s i_{qg,k}) \tag{10}$$

$$\frac{di_{qg,k}}{dt} = \frac{1}{L_s} (u_{qg,k} - Ri_{qg,k} - \omega_{s,k}L_s i_{dg,k} - \omega_{s,k}\psi_{m,k}) \tag{11}$$

where  $\omega_s = p\omega_g$  is the electrical generator speed.

The mechanical subsystem dynamics of the PMSG can be expressed by

$$\frac{d\omega_{g,k}}{dt} = \frac{1}{J} (T_{t,k} - T_{g,k} - T_{f,k}) \tag{12}$$

The PMSG torque can be evaluated by

$$T_{g,k} = 1.5p\psi_{m,k}i_{qg,k} \tag{13}$$

The data specifications of the wind conversion system are shown in Table 5, in appendix A.

**III. MODELING OF BATTERY, CONVERTERS, DC BUS AND MOTOR-PUMP UNIT**

**A. BATTERY MODELING**

The battery is utilized to handle the surplus power and compensate the wind energy shortage. In addition, to avoid the system malfunctions due to the wind intermittence behavior, a battery storage system must be incorporated. As stated in [52], [53], the battery voltage balance can be represented by

$$\begin{aligned} U_{bat,k} &= I_{bat,k}R_t + I_{b,k}R_e + U_{cb,k} \\ &= I_{bat,k}R_t + I_{s,k}R_s + U_{cs,k} \end{aligned} \tag{14}$$

The battery voltage dynamics can be also expressed in the matrix form by

$$\begin{aligned} \begin{bmatrix} \frac{dU_{cb,k}}{dt} \\ \frac{dU_{cs,k}}{dt} \\ \frac{dU_{bat,k}}{dt} \end{bmatrix} &= \begin{bmatrix} Z_{11} & Z_{12} & Z_{13} \\ Z_{21} & Z_{22} & Z_{23} \\ Z_{31} & Z_{32} & Z_{33} \end{bmatrix} \cdot \begin{bmatrix} U_{cb,k} \\ U_{cs,k} \\ U_{bat,k} \end{bmatrix} \\ &+ \begin{bmatrix} \frac{R_s}{C_b(R_e + R_s)} \\ \frac{R_b}{C_s(R_e + R_s)} \\ \frac{R_s}{B} \end{bmatrix} \cdot I_{bat,k} \end{aligned} \tag{15}$$

where  $Z_{11} = \frac{-1}{C_b(R_e + R_s)}$ ,  $Z_{12} = \frac{1}{C_b(R_e + R_s)}$ ,  $Z_{13} = 0$ ,  $Z_{21} = \frac{1}{C_s(R_e + R_s)}$ ,  $Z_{22} = \frac{-1}{C_s(R_e + R_s)}$ ,  $Z_{23} = 0$ ,  $Z_{31} = \frac{-R_s}{C_b(R_e + R_s)^2} + \frac{R_e}{C_s(R_e + R_s)^2} - \frac{R_s^2}{C_b R_e (R_e + R_s)^2} + \frac{R_s}{C_s(R_e + R_s)^2}$ ,  $Z_{32} = 0$ ,  $Z_{33} = \frac{R_s}{C_b R_e (R_e + R_s)} - \frac{1}{C_s(R_e + R_s)}$ ,  $B = \frac{R_e^2}{C_b(R_e + R_s)^2} - \frac{R_s R_t}{C_b(R_e + R_s)} + \frac{R_s R_e}{C_s(R_e + R_s)^2} + \frac{R_t}{C_s(R_e + R_s)}$ .

The battery specifications are presented in Table 6 in Appendix A.

**B. MODELING OF POWER CONVERTERS AND DC BUS**

Figure 1 illustrates an overview of the wind generation based water pumping system. The system consists of three main parts: the wind turbine system, the battery system and the water pumping system, in addition to the DC link unit which represents the power port that links the different units. In the figure, it can be noticed that there is a machine side converter (MSC) which acts as a controlled rectifier to handle the generator power to the other units through the DC link. Also there is the motor-pump inverter (MPI) which regulates the operation of the IM that manages the pump operation. There is also a bi-directional DC/DC power converter which is used to regulate the battery operation.

Consequently, the models of these converters must be constructed to ensure the proper power flow. Generally, the MSC and MPI have a faster dynamic compared with the wind dynamics. For this reason, it is appropriate to identify solely the low-operating frequency of the converters variables in order to describe the wind system dynamics [54], [55]. Consequently, a continuous equivalent converter model is used to represent the current and voltage dynamic states.

According to these assumptions, the modulated voltages of the MSC are determined by

$$\begin{bmatrix} u_{dg,k} \\ u_{qg,k} \end{bmatrix} = \frac{U_{dc,k}}{2} \begin{bmatrix} u_{dg,k}^c \\ u_{qg,k}^c \end{bmatrix} \tag{16}$$

where  $U_{dc}$  is the DC bus voltage, and  $u_{dg}^c$  and  $u_{qg}^c$  are the MSC control signals.

where  $i_{ds,k}$  and  $i_{qs,k}$  are the IM  $d$ - $q$  currents. Meanwhile,  $e_d^c$  and  $e_q^c$  are the MPI inverter control signals.

In addition, the MPI modulated voltages can be calculated by

$$\begin{bmatrix} e_{d,k} \\ e_{q,k} \end{bmatrix} = \frac{U_{dc,k}}{2} \begin{bmatrix} e_{d,k}^c \\ e_{q,k}^c \end{bmatrix} \tag{17}$$

Then, the modulated generator current  $I_{m1}$  shown in Fig. 1 can be evaluated as following

$$I_{m1,k} = \frac{1}{2} (u_{dg,k}^c i_{dg,k} + u_{qg,k}^c i_{qg,k}) \tag{18}$$

Similarly, the modulated current of the MPI inverter ( $I_{m,inv}$ ), can be expressed by

$$I_{m,inv,k} = \frac{1}{2} (e_{d,k}^c i_{ds,k} + e_{q,k}^c i_{qs,k}) \tag{19}$$

The bi-directional DC/DC power converter illustrated in Fig. 1 is also utilized to regulate the charging/discharging process for the battery storage system (BSS). An inductor  $L_{bat}$  is used to attenuate the battery current harmonics. Similar to the MSC and MPI, a continuous model is used for the bi-directional converter, and consequently the modulated voltage and current for the DC/DC converter are calculated by

$$U_{m,bat,k} = m_{bat,k} U_{dc,k} \tag{20}$$

$$I_{m,bat,k} = m_{bat,k} I_{bat,k} \tag{21}$$

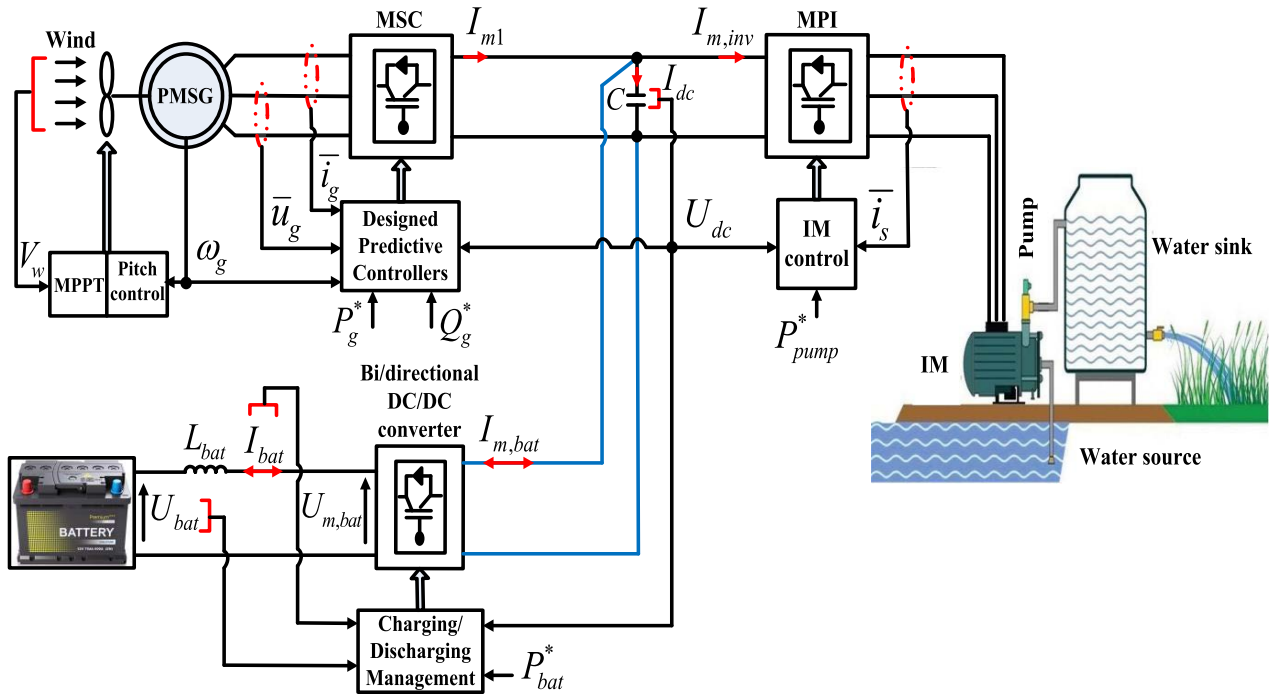


FIGURE 1. Layout of hybrid power system (HPS).

From (18) and (19), the dynamics of DC link can be described by the following relationship

$$C \frac{dU_{dc,k}}{dt} = I_{dc,k} = I_{m1,k} + I_{m,bat,k} - I_{m,inv,k} \quad (22)$$

The control systems design for the MSC and MPI power converters is comprehensively explained in Sec. V.

### C. MODELING OF MOTOR-PUMP UNIT

The pump is operated with the help of an IM. The IM equivalent model can be constructed as given in [56], in which all variables are defined in a frame rotates with a similar speed to the rotor flux vector  $\omega_{\bar{\psi}_r}$ .

Then, the IM dynamics can be described by

$$\frac{d\bar{\psi}_{s,k}^{rf}}{dt} = \bar{u}_{s,k}^{rf} - R_p \bar{i}_{s,k}^{rf} - j\omega_{\bar{\psi}_r} \bar{\psi}_{s,k}^{rf} \quad (23)$$

$$\frac{d\bar{\psi}_{r,k}^{rf}}{dt} = -R_r \bar{i}_{r,k}^{rf} - j \left( \overbrace{\omega_{\bar{\psi}_r,k}^{slip,k}}^{\omega_{\bar{\psi}_r,k} - \omega_{me,k}} \right) \bar{\psi}_{r,k}^{rf} \quad (24)$$

$$\frac{d\omega_{me,k}}{dt} = \frac{n_p}{J_m} (T_{e,k} - T_{l,k}) \quad (25)$$

where  $\omega_{me} = n_p \omega_m$  is the electrical rotor speed,  $n_p$  is the pole pairs and  $\omega_m$  is the mechanical rotor speed. The superscript  $^{rf}$  refers to the rotor flux rotating frame.

The torque  $T_{e,k}$  can be evaluated by

$$\begin{aligned} T_{e,k} &= 1.5n_p \frac{L_m}{\sigma L_s L_r} \bar{\psi}_{s,k}^{rf} \times \bar{\psi}_{r,k}^{rf} \\ &= 1.5n_p \frac{L_m}{\sigma L_s L_r} (\psi_{qs,k}^{rf} \psi_{dr,k}^{rf} - \psi_{ds,k}^{rf} \psi_{qr,k}^{rf}) \end{aligned} \quad (26)$$

where  $\sigma = 1 - (L_m^2 / L_s L_r)$  is the leakage factor.

The output mechanical power on the IM shaft equalizes the absorbed power by the pump, which can be evaluated by

$$P_{pump,k} = K_L \omega_{m,k}^3 \quad (27)$$

where  $K_L$  is the speed-torque coefficient.

The beneficial pump power ( $P_h$ ) can be represented by

$$P_{h,k} = \eta P_{pump,k} = DgH_k Q_k \quad (28)$$

where  $D$  is the density ( $k_g/m^3$ ),  $g$  is the gravity acceleration ( $m^2/s$ ).

The water volume can be calculated as

$$V_k = Q_k \Delta T \quad (29)$$

To evaluate the water level ( $H$ ) inside the tank, the following relationship is used

$$\frac{dV_k}{dt} = S \frac{dH_k}{dt} = Q_{i,k} - Q_{o,k} \quad (30)$$

where  $Q_i$  and  $Q_o$  are the water flow entering and leaving the tank, respectively. And  $S$  is the tank area.

### IV. SUPERVISORY HIERARCHICAL CONTROL

To control and supervise the operation of the hybrid power system (HPS), a supervisory hierarchical control is represented as shown in Fig. 2. In this system, there are three main phases that can be described as follows

- In the first phase, a strategy for sharing the power (PSS) is used to generate the command power signals for each unit in the HPS in order to fulfill the motor-pump unit requirements. The power management strategy (PMS) is also implemented in this step to

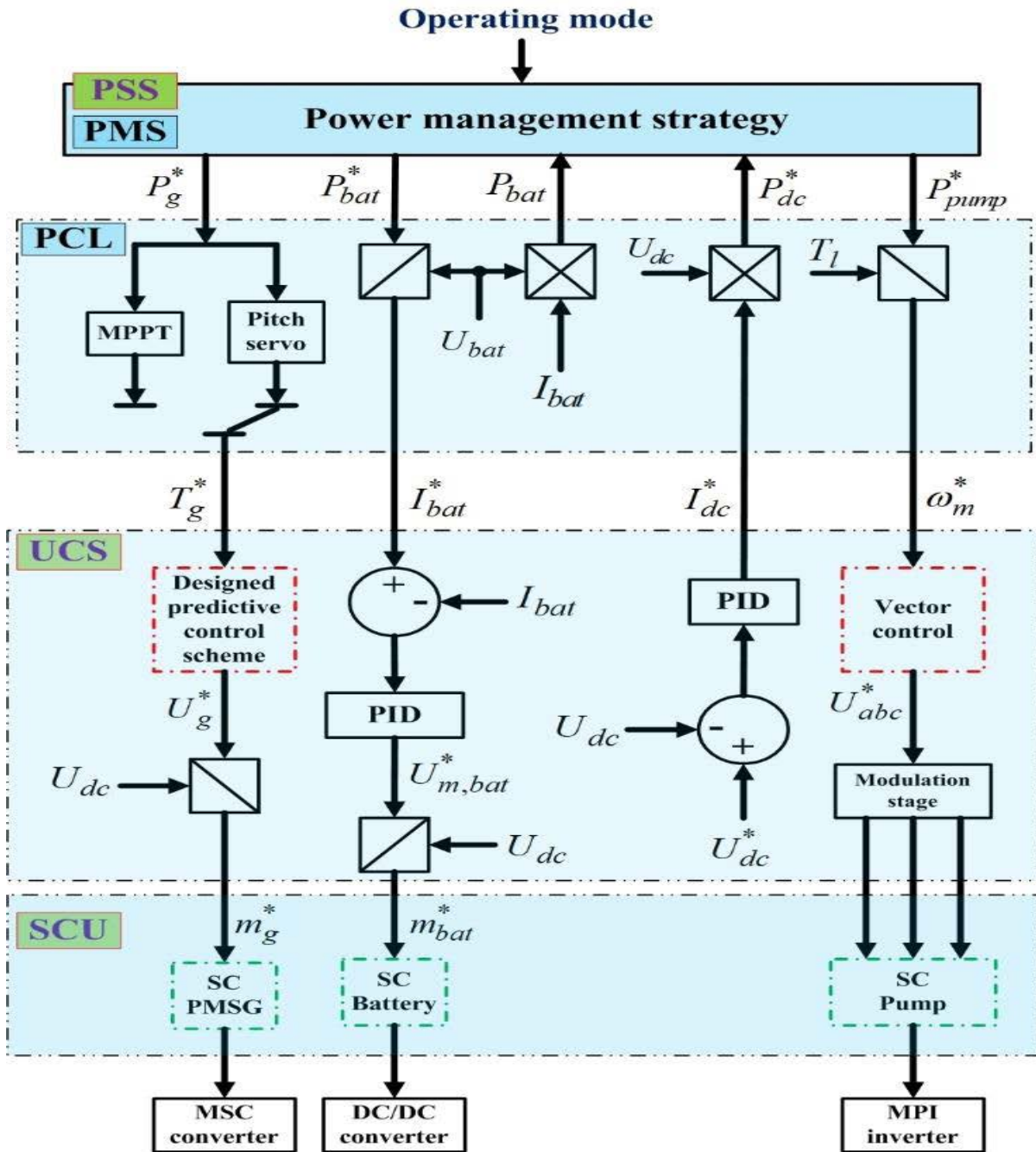


FIGURE 2. Supervisory power control system.

achieve the balance between the power production and consumption.

- In the second phase, the internal control of each system unit is applied. So it is entitled ‘units control stage’ (UCS). During this step, the modulation indices ( $m$ ) for each power converter used in the HPS are generated.
- In the third phase, the switching management unit (SMU) is used to provide the switching signals for the specified converters.

### A. POWER SHARING STRATEGY (PSS)

Delivering the power to the water pump must follow the operation strategy and the connection architecture. Therefore, to maintain the system power balance, a PSS strategy is structured. The PSS consists of two subsystems: the power control level (PCL) and the power management strategy (PMS).

#### 1) POWER CONTROL LEVEL (PCL)

As shown in Fig. 2, the PCL is used to provide four reference values: generator torque reference ( $T_g^*$ ), battery current

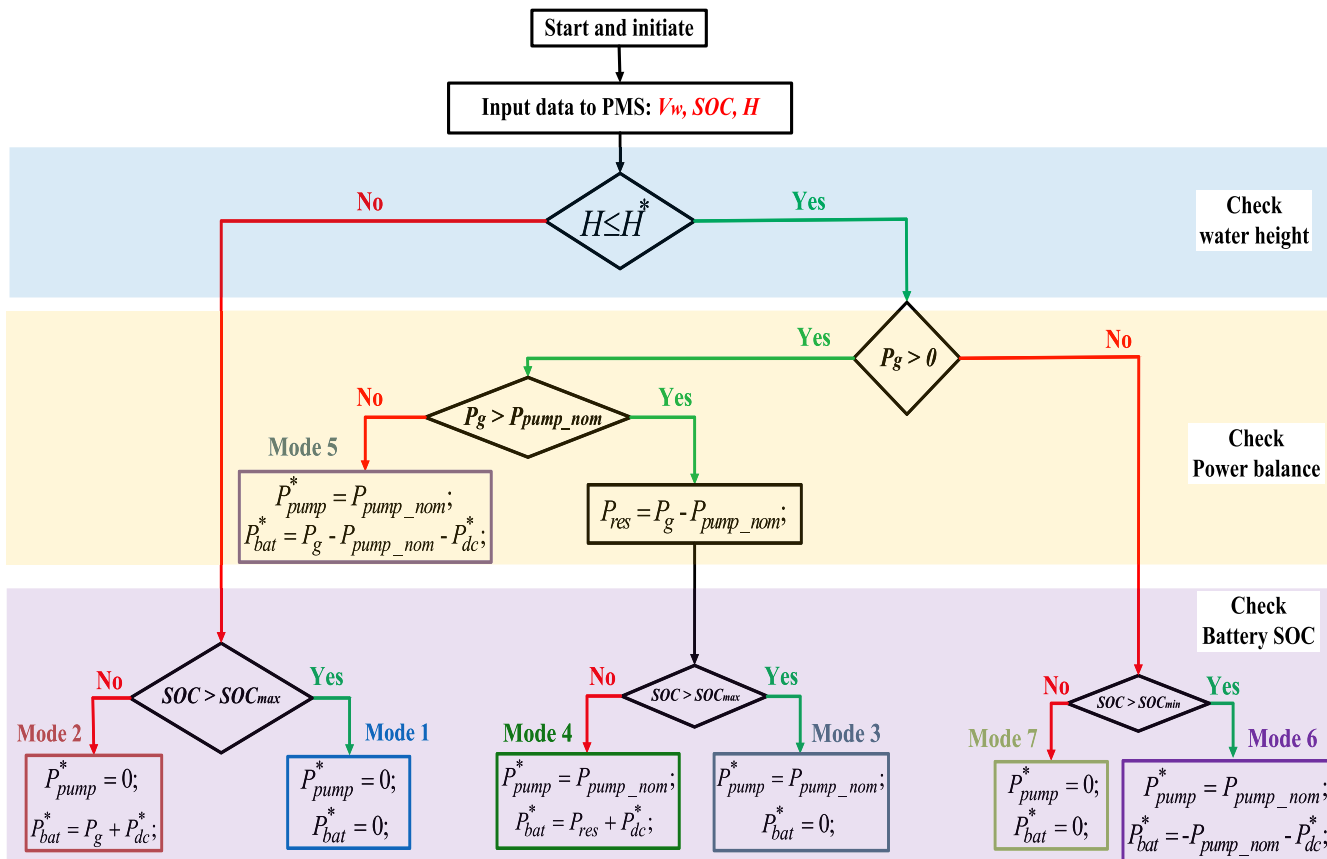


FIGURE 3. Power management system (PMS).

reference ( $I_{bat}^*$ ), DC link current reference ( $I_{dc}^*$ ), and IM speed reference ( $\omega_m^*$ ). These references are extracted from the interchanged power between the system units and the DC link. The power flow management is realized via utilizing the model expressions in order to identify the reference power ( $P_{pump}^*$ ) besides the DC link reference power ( $P_{dc}^*$ ) while estimating the available wind power to be delivered to the generator ( $P_g^*$ ).

2) POWER MANAGEMENT STRATEGY (PMS)

The PMS strategy is concerned with dispatching the powers between the various system units to fulfill the power requirements of the pumpingsystem. The generator power ( $P_g$ ), the actual ( $H$ ) and desired ( $H^*$ ) heights in the water sink tank, and the battery SOC are the inputs to the PMS. These data besides the function of the battery storage system (BSS) (even with the excess or lack of developed power) will identify the system working modes as shown in Fig. 3. Essentially, the specified modes are depicted to ensure tracking the desired power levels of the wind turbine, the pump and the BSS system. This is in addition to ensuring the stability of the pump power flow respecting to the DC bus voltage, the limits of BSS ( $SOC_{max}, SOC_{min}$ ) and pump specifications as obviously shown in Fig. 3.

The detailed description of each operating mode in Fig. 3 is presented as follows:

a: OPERATING MODE 1

In this mode, the water level ( $H$ ) inside the tank is higher or similar to the predefined height  $H^*$  (Tank is filled). Furthermore, the power delivered is higher than the demanded by the pump, that is here zero ( $P_{pump}^* = 0$ ), and the battery is with full charge ( $SOC > SOC_{max}$ ). As a result, the surplus power is disregarded without operating the pump. The mathematical relationships that represent the first mode are expressed by

$$P_{pump}^* = 0 \quad \text{and} \quad P_{bat}^* = 0 \tag{31}$$

b: OPERATING MODE 2

This mode is relevant to the case at which the water tank is fully occupied, with the generated power from the PMSG larger than the demanded power and with a SOC lower than the maximum SOC ( $SOC < SOC_{max}$ ). For this case, the surplus power is received by the BSS until the battery reaches its ultimate SOC level. The relations that describe this mode are given by

$$P_{pump}^* = 0 \quad \text{and} \quad P_{bat}^* = P_g \tag{32}$$

c: OPERATING MODE 3

In this mode, the water reservoir is not completely occupied; meanwhile the battery charging is complete. Additionally, the generator's power is capable of operating the pump until



the water level reaches to its maximum limit. The generated power supply the nominal pump power ( $P_{pump\_nom}$ ). Consequently, the powers at this stage are represented as

$$P_{pump}^* = P_{pump\_nom} \quad \text{and} \quad P_{bat}^* = 0 \quad (33)$$

**d: OPERATING MODE 4**

In this mode, the generated power is adequate, the water reservoir is not totally occupied; in addition, the battery charging is not complete. The system continues to work in order to fill the tank and in case of having a surplus power, the BSS will absorb it as long as the battery SOC stays in the permissible range. Therefore, the battery is under the charging mode. The power relationships in this mode are described by

$$P_{pump}^* = P_{pump\_nom} \quad \text{and} \quad P_{bat}^* = P_g - P_{pump\_nom} + P_{dc}^* \quad (34)$$

**e: OPERATING MODE 5**

In this mode, the PMSG does not provide the sufficient power to operate the pump. Consequently, the BSS takes care of this action via compensating the power difference until the water tank is filled. The power relationships at this stage are expressed by

$$\begin{aligned} P_{pump}^* &= P_{pump\_nom} \quad \text{and} \\ P_{bat}^* &= P_g - P_{pump\_nom} - P_{dc}^* \end{aligned} \quad (35)$$

**f: OPERATING MODE 6**

In this stage, the pump is operated completely from the BSS because of missing the wind power. The battery is running under the discharging mode. As a result, the power balance can be described by

$$\begin{aligned} P_{pump}^* &= P_{pump\_nom} \quad \text{and} \\ P_{bat}^* &= -P_{pump\_nom} - P_{dc}^* \end{aligned} \quad (36)$$

**g: OPERATING MODE 7**

In this mode, the water pump is disconnected from the HPS, and the powers can be expressed by

$$P_{pump}^* = 0 \quad \text{and} \quad P_{bat}^* = 0 \quad (37)$$

**V. UNITS CONTROL STAGE (UCS)**

As illustrated in Fig. 2, the UCS contains the separate control for each unit in the HPS system. Thus, the following subsections are devoted to provide a detailed description for the used control strategies.

**A. CONTROL OF PMSG**

The PMSG and its wind turbine driving system constitute the core of the HPS, and for this reason, different control algorithms are utilized to analyze the PMSG and outline the most appropriate in between to achieve the optimal power capturing while ensuring high power quality through limiting the ripples and generated current harmonics. Four predictive controllers are formulated to manage the PMSG performance. The mechanism by which each control works is described as follows:

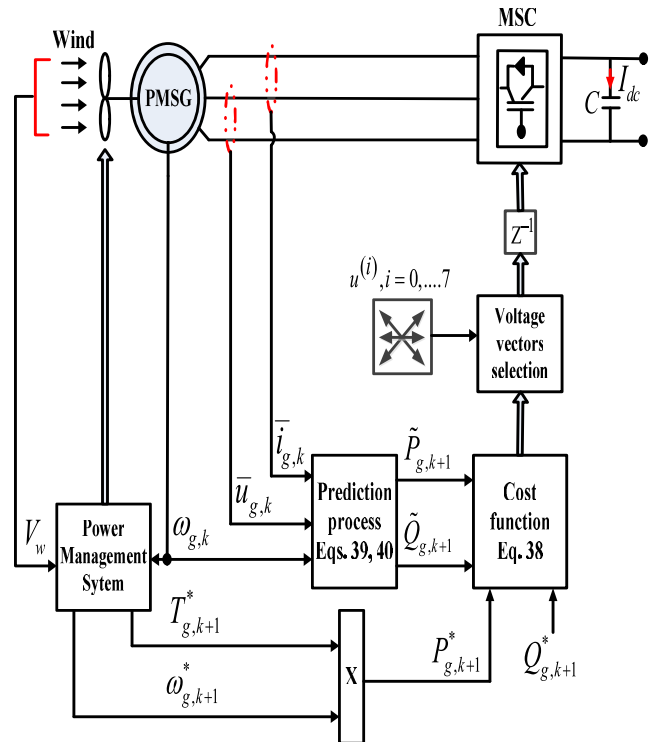


**FIGURE 4. Layout of MP DPC for PMSG.**

**1) DESIGN OF MP DPC FOR PMS**

The MP DPC operation stands on controlling the active and reactive powers of the PMSG. The core operation of the MP DPC is performed by a CF that handles the deviations of the actual predicted powers from their references. The CF also uses a scaling factor  $S_f = \frac{P_{nom}}{Q_{nom}}$  to give a weight for the reactive power corresponding to the active power. Consequently, the MP DPC cost function is represented by

$$C_{k+1}^i = \left| P_{g,k+1}^* - \tilde{P}_{g,k+1} \right|^i + S_f \left| Q_{g,k+1}^* - \tilde{Q}_{g,k+1} \right|^i \quad (38)$$

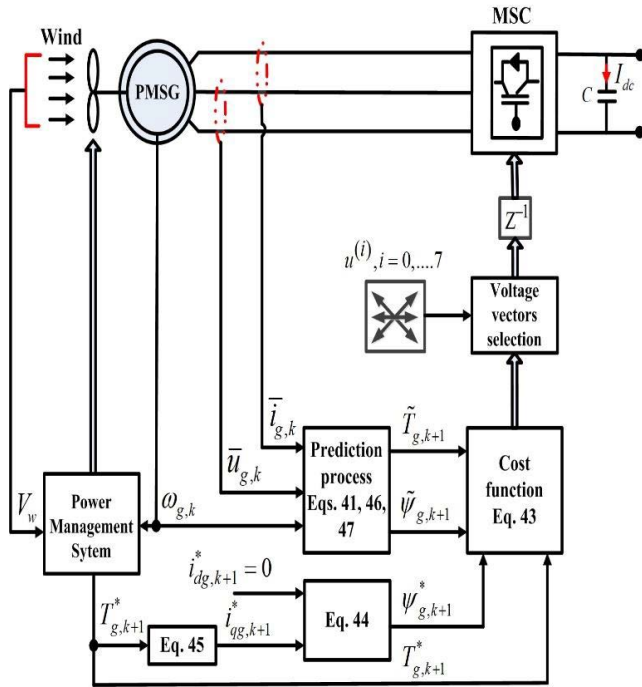
where the superscript  $i$  identifies the voltage index. The reference power  $Q_{g,k+1}^*$  is set to zero, while the reference active power ( $P_{g,k+1}^* = T_{g,k+1}^* * \omega_{g,k+1}^*$ ) is derived from the wind turbine driving system. Furthermore, the predicted powers  $\tilde{P}_{g,k+1}$  and  $\tilde{Q}_{g,k+1}$  can be evaluated by

$$\tilde{P}_{g,k+1} = 1.5 \left( u_{dg,k+1} \tilde{i}_{dg,k+1} + u_{qg,k+1} \tilde{i}_{qg,k+1} \right) \quad (39)$$

$$\tilde{Q}_{g,k+1} = 1.5 \left( u_{qg,k+1} \tilde{i}_{dg,k+1} - u_{dg,k+1} \tilde{i}_{qg,k+1} \right) \quad (40)$$

where  $\tilde{i}_{dg,k+1}$  and  $\tilde{i}_{qg,k+1}$  are the predicted  $d$ - $q$  currents of PMSG which are calculated using (10) and (11) as following

$$\begin{aligned} \tilde{i}_{dg,k+1} &= i_{dg,k} + \left( \frac{di_{dg,k}}{dt} \right) T_s \quad \text{and} \\ \tilde{i}_{qg,k+1} &= i_{qg,k} + \left( \frac{di_{qg,k}}{dt} \right) T_s \end{aligned} \quad (41)$$


**FIGURE 5.** Layout of MP DTC for PMSG.

The  $d$ - $q$  voltage components  $u_{dg,k+1}$  and  $u_{qg,k+1}$  can be evaluated by

$$\begin{aligned} u_{dg,k+1} &= u_{dg,k} + \left( \frac{u_{dg,k} - u_{dg,k-1}}{\Delta T} \right) T_s \quad \text{and} \\ u_{qg,k+1} &= u_{qg,k} + \left( \frac{u_{qg,k} - u_{qg,k-1}}{\Delta T} \right) T_s \end{aligned} \quad (42)$$

Thus, after calculating the terms of (38), the control starts to evaluate the cost function value at each instant and identifies the first voltage vectors that minimize its value and apply to the machine terminals. The system layout of the MP DTC is shown in Fig. 4.

## 2) DESIGN OF MP DTC FOR PMSG

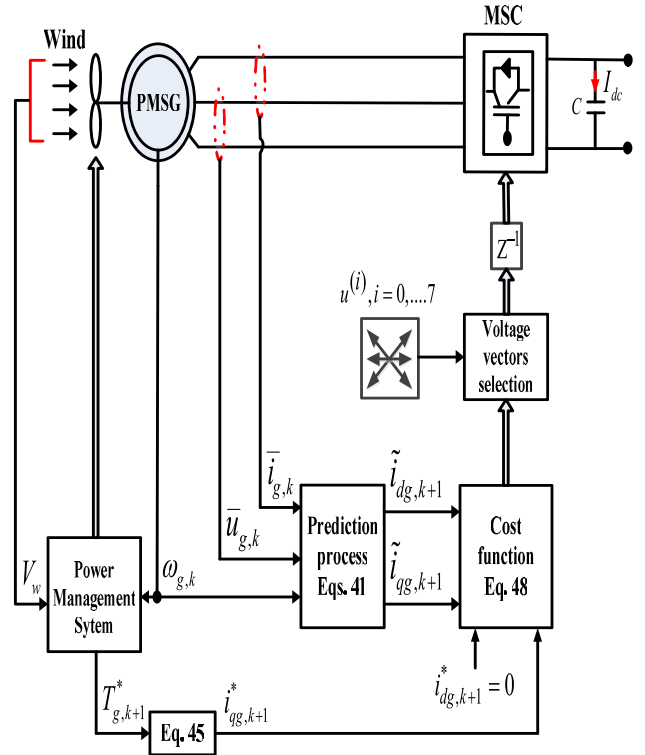
The MP DTC operation aims to managing the flux and torque of the PMSG. Accordingly, the controller utilizes a CF combining the flux and torque errors, through which the optimal voltages can be obtained. The CF substitutes the role of hysteresis regulators and look-up tables used in DTC. Following this fact, the CF of the MP DTC is formulated by

$$C_{k+1}^i = \left| T_{g,k+1}^* - \tilde{T}_{g,k+1} \right|^i + S_f' \left| \psi_{g,k+1}^* - \tilde{\psi}_{g,k+1} \right|^i \quad (43)$$

where  $T_{g,k+1}^*$  and  $\psi_{g,k+1}^*$  are the torque and flux reference values.  $S_f' = \frac{T_{nom}}{\psi_{nom}}$  is the scaling factor. In addition,  $\tilde{T}_{g,k+1}$  and  $\tilde{\psi}_{g,k+1}$  are the predicted torque and flux.

The torque reference  $T_{g,k+1}^*$  is provided by the wind power system explained earlier in Sec. II; while the flux reference  $\psi_{g,k+1}^*$  is calculated utilizing the  $d$ - $q$  command currents as following

$$\psi_{g,k+1}^* = \sqrt{\left( L_s i_{dg,k+1}^* + \psi_{m,k+1} \right)^2 + \left( L_s i_{qg,k+1}^* \right)^2} \quad (44)$$


**FIGURE 6.** MP CC scheme for PMSG.

The current reference  $i_{dg,k+1}^*$  is kept to zero; while the reference  $i_{qg,k+1}^*$  is calculated by

$$i_{qg,k+1}^* = \frac{T_{g,k+1}^*}{1.5p\psi_{m,k+1}} \quad (45)$$

The predicted torque and flux signals in (43) are computed by

$$\begin{aligned} \tilde{T}_{g,k+1} &= 1.5p\psi_{m,k+1}\tilde{i}_{qg,k+1} \quad (46) \\ \tilde{\psi}_{g,k+1} &= \sqrt{\left( L_s \tilde{i}_{dg,k+1} + \psi_{m,k+1} \right)^2 + \left( L_s \tilde{i}_{qg,k+1} \right)^2} \quad (47) \end{aligned}$$

The predicted currents  $\tilde{i}_{dg,k+1}$  and  $\tilde{i}_{qg,k+1}$  are calculated using (41).

Accordingly, the MP DTC starts to evaluate (43), and identifies the optimal voltage which minimizes (43) and apply it. The MP DTC schematic diagram is shown in Fig. 5.

## 3) DESIGN OF MP CC FOR PMSG

The MP CC operation aims to regulating the  $d$ - $q$  current components of PMSG in order to indirectly control the flux and torque, respectively [48]. The MP CC approach replaces the PI current regulators used in classic vector control approach with a CF which combines the deviations of the  $d$ - $q$  currents as following

$$C_{k+1}^i = \left| i_{dg,k+1}^* - \tilde{i}_{dg,k+1} \right|^i + \left| i_{qg,k+1}^* - \tilde{i}_{qg,k+1} \right|^i \quad (48)$$

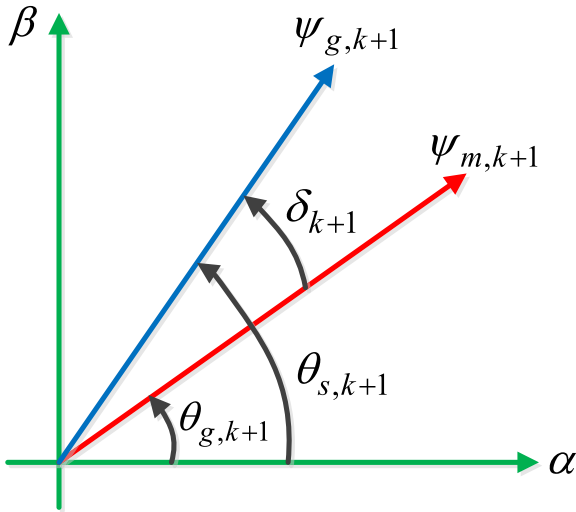


FIGURE 7. Allocation of fluxes in space.

The current reference  $i_{dg,k+1}^*$  is kept to zero to ensure unity pf operation; meanwhile the reference  $i_{qg,k+1}^*$  is obtained using (45). Alternatively, the predicted currents  $\tilde{i}_{dg,k+1}$  and  $\tilde{i}_{qg,k+1}$  can be evaluated using (41).

After evaluating the value of (48) at each sampling time, the MP CC specifies the optimal voltage value which makes (48) with zero value and apply it. A layout for the MP CC approach is shown in Fig 6.

#### 4) PROPOSED PVC FOR PMSG

The main deficiency in the CF used by the MP DPC and MP DTC schemes is the utilization of estimated variables, which consume the time, and consequently increases the number of commutations. This is in addition to the issue of scaling factor. As an attempt to avoid these deficiencies, a predictive voltage control (PVC) technique is presented. The designed PVC utilizes a CF of two matched parts without adding a weighting scale. In addition, the variables used in the cost function do not require an estimation, which saves the computation time and limits the switching losses. The cost function of the proposed PVC can be expressed by

$$C_{k+1}^i = \left| u_{dg,k+1}^* - u_{dg,k+1} \right|^i + \left| u_{qg,k+1}^* - u_{qg,k+1} \right|^i \quad (49)$$

The FCS is used to generate the actual voltages  $u_{dg,k+1}$  and  $u_{qg,k+1}$  in (49). This is accomplished via processing the switching states generated from the controller without using a PWM scheme. Furthermore, the reference voltages  $u_{dg,k+1}^*$  and  $u_{qg,k+1}^*$  are determined using a designed flux and torque regulators. The tuning of these regulators is accomplished as follows:

Considering the flux orientation concept, the PMSG flux should be aligned to the  $q$ -axis of the rotating frame. Consequently, the following relationships are obtained

$$\psi_{dg,k+1} = |\tilde{\psi}_{g,k+1}| \quad \text{and} \quad \psi_{qg,k+1} = 0.0 \quad (50)$$

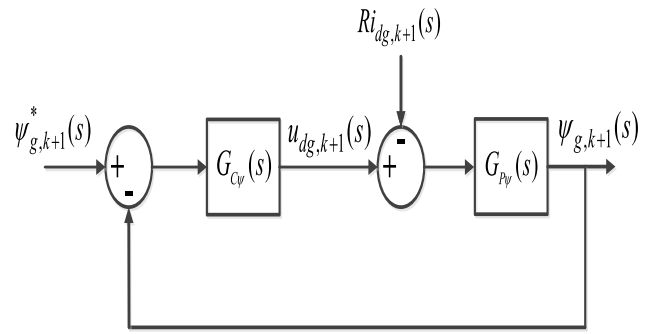


FIGURE 8. Closed loop flux control model.

By replacing from (50) into (10) and (11), it gives

$$u_{dg,k+1} = Ri_{dg,k+1} + \frac{d|\tilde{\psi}_{g,k+1}|}{dt} \quad (51)$$

$$u_{qg,k+1} = Ri_{qg,k+1} + \omega_{s,k+1} |\tilde{\psi}_{g,k+1}| \quad (52)$$

From (51) and by neglecting the voltage drop on  $R$ , the flux can be controlled thoroughly by the voltage  $u_{dg,k+1}$ .

From Fig. 7 which represents the space displacements of the stator flux  $\tilde{\psi}_{g,k+1}$  and rotor flux  $\tilde{\psi}_{m,k+1}$  vectors, the angular frequency of stator flux ( $\omega_{s,k+1}$ ) can be calculated by

$$\omega_{s,k+1} = \omega_{g,k+1} + \frac{d\delta_{k+1}}{dt} \quad (53)$$

where  $\delta_{k+1}$  is the torque angle.

The current  $i_{qg,k+1}$  in (52) can be calculated by

$$i_{qg,k+1} = \frac{T_{g,k+1}}{1.5p |\tilde{\psi}_{g,k+1}|} \quad (54)$$

Then, by substituting from (53) and (54) into (52), it results in

$$u_{qg,k+1} = R \frac{T_{g,k+1}}{1.5p |\tilde{\psi}_{g,k+1}|} + \left( \omega_{g,k+1} + \frac{d\delta_{k+1}}{dt} \right) |\tilde{\psi}_{g,k+1}| \quad (55)$$

From (55), it is obvious that the torque management can be achieved via managing the  $q$ -axis voltage  $u_{qg,k+1}$ .

Accordingly, the command voltages required by (49) can be determined using the following expressions

$$u_{ds,k+1}^* = \left( K_{P\psi} + \frac{K_{I\psi}}{s} \right) (\psi_{g,k+1}^* - \tilde{\psi}_{g,k+1}) \quad (56)$$

$$u_{qs,k+1}^* = \left( K_{PT} + \frac{K_{IT}}{s} \right) (T_{g,k+1}^* - \tilde{T}_{g,k+1}) \quad (57)$$

where  $K_{P\psi}$ ,  $K_{I\psi}$ ,  $K_{PT}$  and  $K_{IT}$  are the parameters of flux and torque controllers, accordingly.

Figure 8 formulates the closed flux control loop, which is evaluated by deriving the Laplace transform of (51).

In Fig. 8, the plant and controller transfer functions ( $G_{P\psi}(s)$  and  $G_{C\psi}(s)$ ) are defined as

$$G_{P\psi}(s) = \frac{1}{s} \quad (58)$$

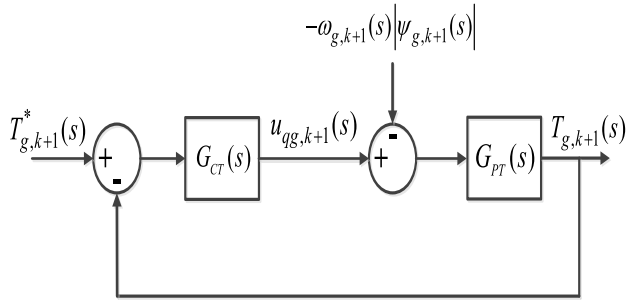


FIGURE 9. Closed loop torque control model.

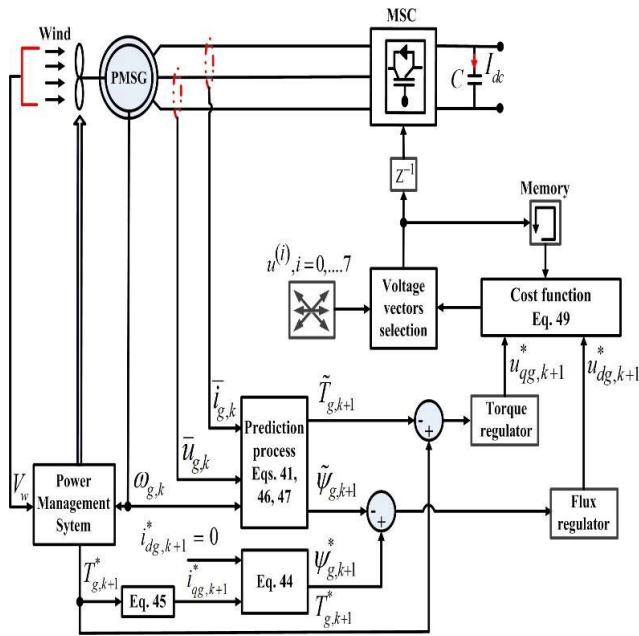


FIGURE 10. Proposed PVC layout.

$$G_{C\psi}(s) = \frac{K_{P\psi}s + K_{I\psi}}{s} \quad (59)$$

Accordingly, from (58) and (59), the transfer function which governs the flux controller can be then evaluated by

$$G_{\psi}(s) = \frac{G_{P\psi}(s)G_{C\psi}(s)}{1 + G_{P\psi}(s)G_{C\psi}(s)} = \frac{K_{P\psi}s + K_{I\psi}}{s^2 + K_{P\psi}s + K_{I\psi}} \quad (60)$$

The denominator of (60) formulates the characteristic equation of the controller, which must be with negative roots in order to ensure stable dynamics. Accordingly, the following is obtained

$$s^2 + K_{P\psi}s + K_{I\psi} = 0 \quad (61)$$

Alternatively, the dynamics of a second order model is expressed by

$$s^2 + 2\omega_n\xi s + \omega_n^2 = 0 \quad (62)$$

where  $\omega_n$  and  $\xi$  are the system frequency and damping factor.

By comparing, (61) and (62), the coefficients of flux regulator are obtained by

$$K_{P\psi} = 2\omega_n\xi \quad \text{and} \quad K_{I\psi} = \omega_n^2 \quad (63)$$

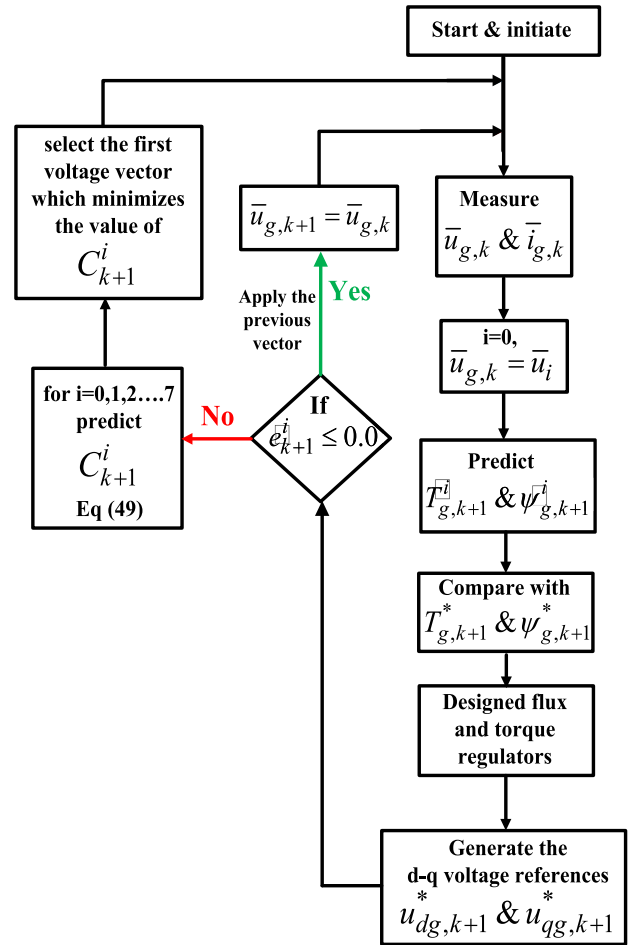


FIGURE 11. Implementation sequence of proposed PVC scheme.

In a same way, the gains of torque controller can be determined via analyzing (55).

From Fig. 8, the torque can be evaluated by

$$T_{g,k+1} = \frac{1.5p}{L_s} |\psi_{m,k+1}| |\bar{\psi}_{g,k+1}| \sin \delta_{k+1} = K_T \sin \delta_{k+1} \quad (64)$$

By differentiating (64) and adding the result to (55), it gives

$$u_{qs,k+1} = \frac{RT_{g,k+1}}{1.5p |\bar{\psi}_{g,k+1}|} + \left( \omega_{g,k+1} + \frac{dT_{g,k+1}}{\Upsilon_T dt} \right) |\bar{\psi}_{g,k+1}| \quad (65)$$

where  $\Upsilon_T = K_T \cos \delta_{k+1}$ .

Applying the Laplace transform on (65), it gives

$$u_{qg,k+1}(s) = \left( \frac{R}{1.5p |\bar{\psi}_{g,k+1}|(s)} + \frac{|\bar{\psi}_{g,k+1}|(s)}{\Upsilon_T(s)} \right) T_{g,k+1}(s) + \omega_{g,k+1}(s) |\bar{\psi}_{g,k+1}|(s) \quad (66)$$

Using (66), the torque control loop can be formulated as in Fig. 9. Where,  $G_{PT}(s)$  and  $G_{CT}(s)$  are the transfer functions of the plant and torque controllers. The functions can be

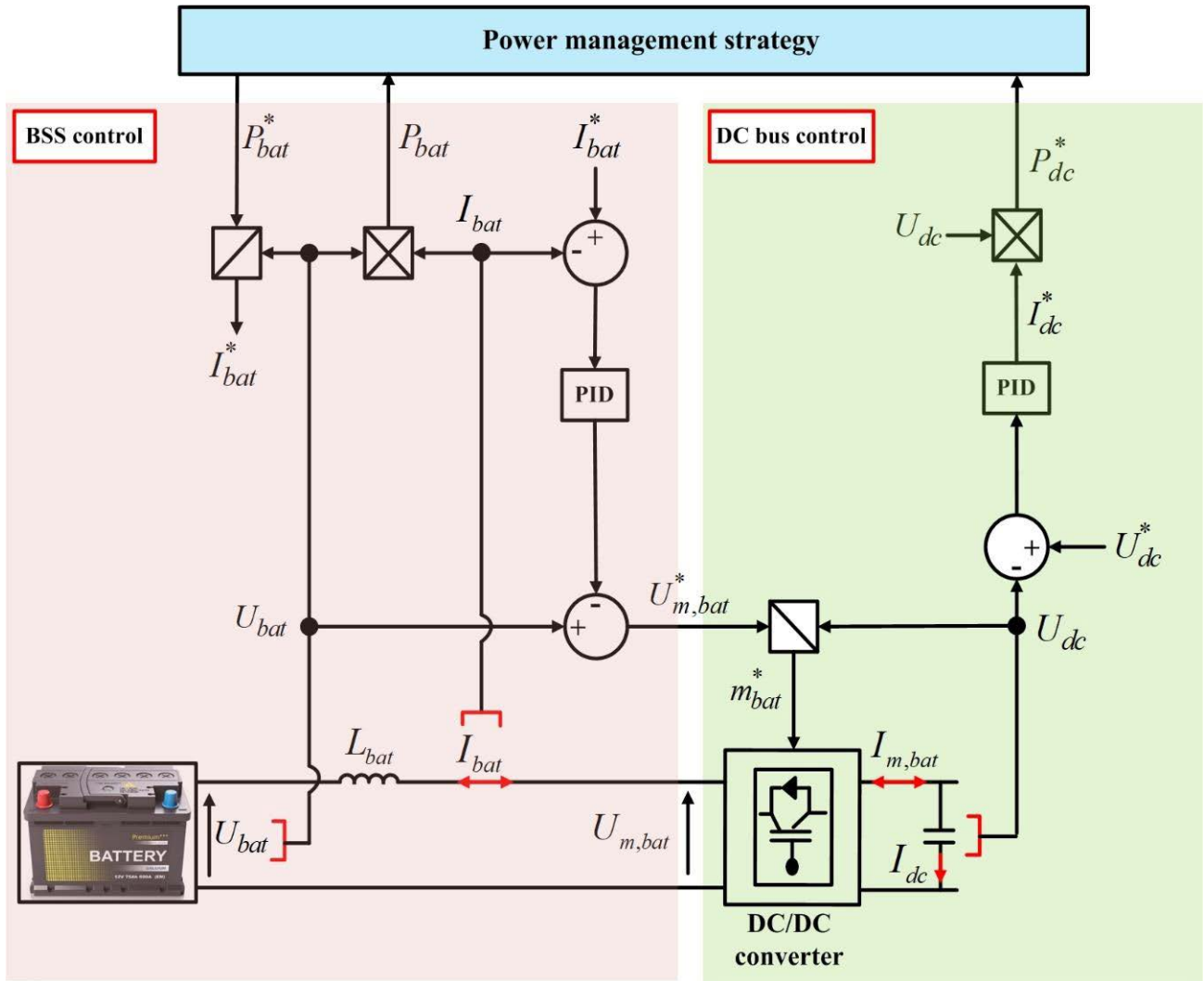


FIGURE 12. Control scheme for BSS and DC bus.

evaluated as following

$$G_{PT}(s) = \frac{1.5p |\bar{\psi}_{g,k+1}|(s) * \Upsilon_T(s)}{R\Upsilon_T(s) + (1.5p |\bar{\psi}_{g,k+1}|^2(s))s} \quad (67)$$

$$G_{CT}(s) = \frac{K_{PT}s + K_{IT}}{s} \quad (68)$$

From Fig. 9, the torque controller dynamics can be represented by the following transfer function as (69), shown at the bottom of the next page.

From (62) and (69) and by comparision, the coefficients of the torque controller are determined as follows

$$K_{PT} = \frac{3p |\bar{\psi}_{g,k+1}|^2 \omega_n \xi - R\Upsilon_T}{1.5p |\bar{\psi}_{g,k+1}| \Upsilon_T}, \quad \text{and} \quad (70)$$

$$K_{IT} = \frac{\omega_n^2 |\bar{\psi}_{g,k+1}|}{\Upsilon_T}$$

After designing the regulators, the reference voltages  $u_{ds,k+1}^*$  and  $u_{qs,k+1}^*$  can be obtained and used in (49). The structure of the proposed PVC is illustrated in Fig. 10.

In order to give a detailed view on the operation mechanism of the proposed PVC, a flow chart is illustrated in Fig. 11 which outlines the implementation stages of the designed control.

### B. CONTROL OF BSS AND DC LINK

When a power shortage or a surplus is present, the BSS is used to regulate the power exchange among the pumping system and the PMSG. As a result, it smoothes out the wind power fluctuations to ensure that the entire system performs properly. A series of batteries, an inductor  $L_{bat}$  acts as a filter and a bi-directional converter formulate the BSS. Fig. 12 illustrates how to manage the power converter and battery current variation. To provide the modulated output battery voltage displayed in Fig. 12 and the duty cycles of

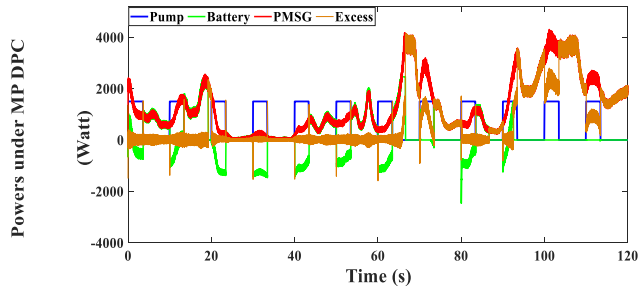


FIGURE 13. Combined power flow under MP DPC.

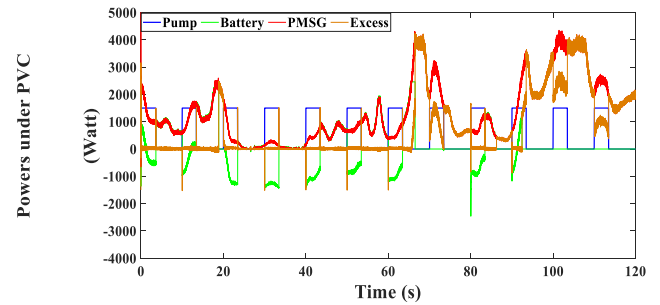


FIGURE 16. Combined power flow under proposed PVC.

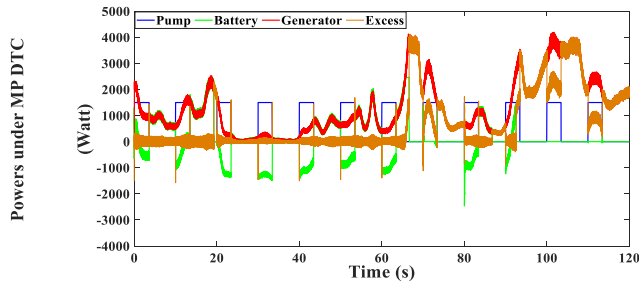


FIGURE 14. Combined power flow under MP DTC.

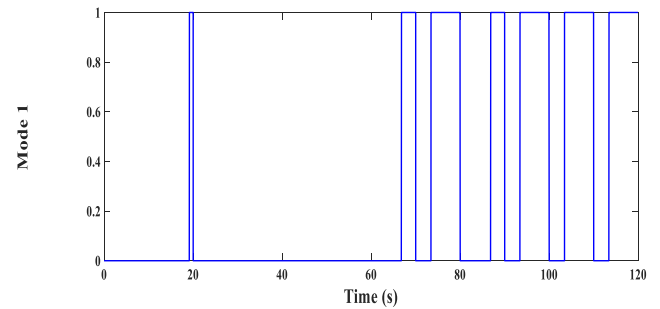


FIGURE 17. Operation mode 1.

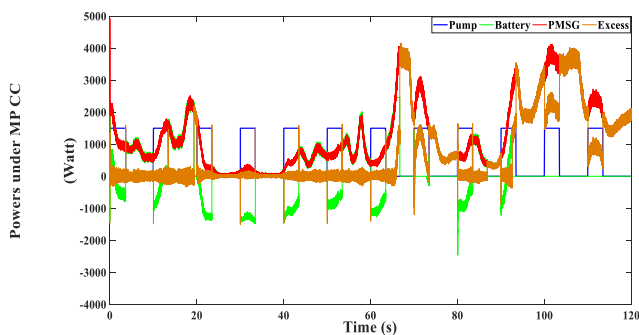


FIGURE 15. Combined power flow under MP CC.

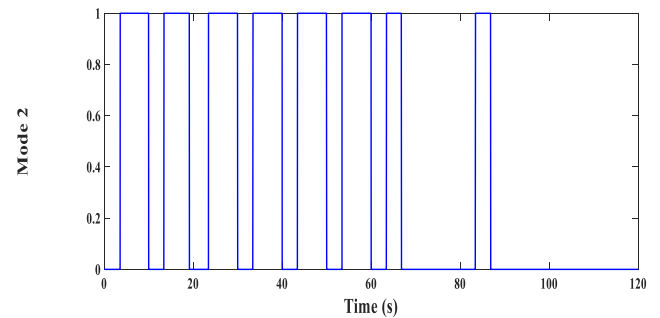


FIGURE 18. Operation mode 2.

the bi-directional converter, an internal control loop for the battery current is utilized.

Due to its slow dynamic, the DC bus voltage is assumed as a constant value. As a result, an outer control loop is used to ensure that the DC link maintains a decent approximation of its reference value regardless of the power exchange between the different units of HPS. Managing the DC voltage plays a significant role in achieving more stable and enhanced system operation. As a result, a PID controller whose input is the battery current error is utilized to compensate the voltage deviation as illustrated in Fig. 12. The design of the two

PID controllers used in Fig. 12 is described in details in the appendix.

### C. CONTROL MOTOR-PUMP UNIT

The water pump operation is managed using an IM drive which is controlled using a field oriented control (FOC) scheme in which the  $d$ -axis of synchronous rotating frame is aligned with the rotor flux vector ( $\psi_{dr,k} = |\bar{\psi}_{r,k}|$  and  $\psi_{qr,k} = 0.0$ ). Furthermore, the motor torque is controlled independently using the  $q$ -axis current ( $i_{qs,k}$ ). On the other side, the rotor flux dynamics is managed using the  $d$ -axis

$$\begin{aligned}
 G_T(s) &= \frac{G_{PT}(s)G_{CT}(s)}{1 + G_{PT}(s)G_{CT}(s)} = \frac{K_{PT}s + K_{IT}}{s^2 + K_{PT}s + K_{IT}} \\
 &= \frac{(1.5p|\bar{\psi}_{g,k+1}|(s) * \Upsilon_T(s)K_{PT})s + 1.5p|\bar{\psi}_{g,k+1}|(s) * \Upsilon_T(s)K_{IT}}{(1.5p|\bar{\psi}_{g,k+1}|^2(s))s^2 + (R\Upsilon_T(s) + 1.5p|\bar{\psi}_{g,k+1}|(s) * \Upsilon_T(s)K_{PT})s + 1.5p|\bar{\psi}_{g,k+1}|(s) * \Upsilon_T(s)K_{IT}} \quad (69)
 \end{aligned}$$

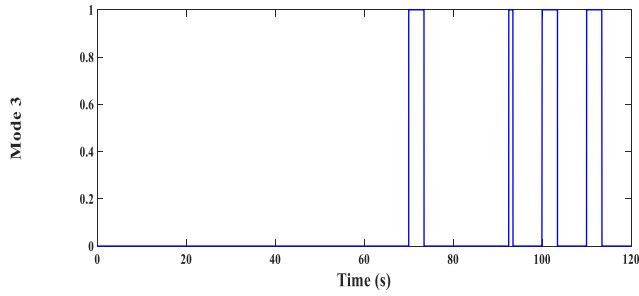


FIGURE 19. Operation mode 3.

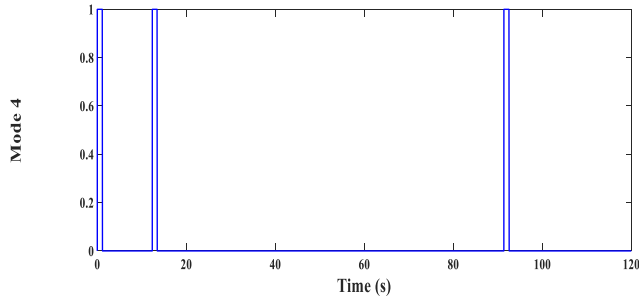


FIGURE 20. Operation mode 4.

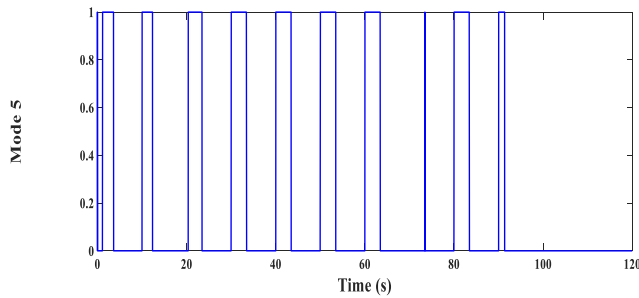


FIGURE 21. Operation mode 5.

current ( $i_{ds,k}$ ). Consequently an independent control of the torque and flux can be achieved, and the IM dynamics can be managed. The relationships between the rotor flux and torque from one side and the direct and quadrature axes stator currents on the other side under FOC are expressed by

$$\psi_{dr,k} = \frac{L_m}{1 + \tau_r s} i_{ds,k} \tag{71}$$

$$T_{e,k} = 1.5n_p \frac{L_m}{L_r} \psi_{dr,k} i_{qs,k} \tag{72}$$

where  $\tau_r$  is the IM rotor time constant.

The management of the IM variables (speed, flux and currents) is achieved through utilizing two PI current controllers in order to keep the actual values following their references.

The parameters of the IM and the PI current controllers' gains are given in Table 1.

Up to this stage, all components of the HPS and its power management and sharing strategy, in addition to the relevant control of each system unit are described in details. In the next section, the test results are demonstrated in which the PMSG and other HPS units dynamics are evaluated considering the

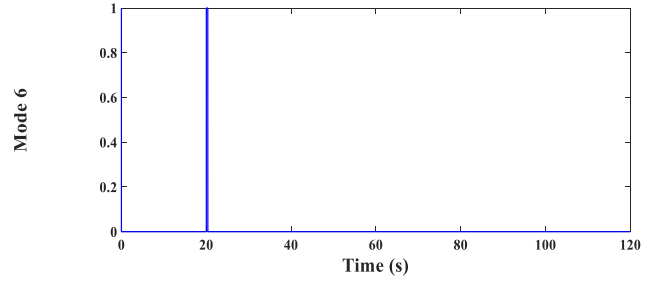


FIGURE 22. Operation mode 6.

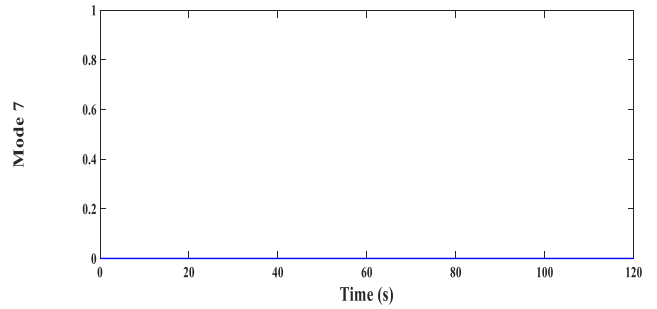


FIGURE 23. Operation mode 7.

TABLE 1. Parameters of IM drive.

$P_n$	3 Kw	$L_r$	0.261 H
$V_{sn}$	380 V	$L_m$	0.245 H
$n_p$	2	$J_m$	0.02 Kg.m <sup>2</sup>
$R_p$	2.3 $\Omega$	$K_{p,i_d}, K_{I,i_d}$	2.4 and 534
$R_r$	1.55 $\Omega$	$K_{p,i_q}, K_{I,i_q}$	2.4 and 534
$L_s$	0.261 H	$K_{p,\omega_m}, K_{I,\omega_m}$	1.78 and 158

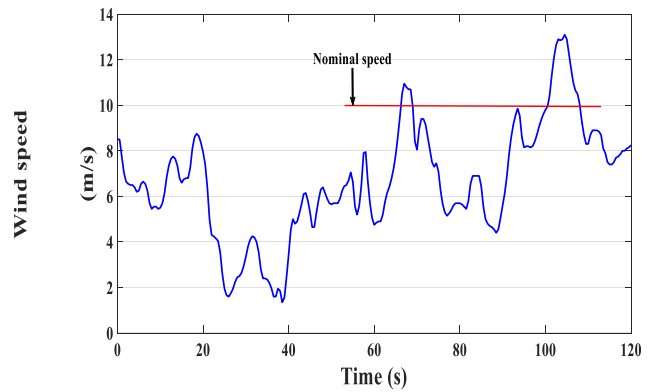


FIGURE 24. Wind speed variation.

previously described predictive controllers with the PMSG, and considering the PMS of all units as well.

## VI. TEST RESULTS

The performance analysis of the HPS and its power management strategy (PMS) and internal unit controls is presented in this section. Firstly, the PMS performance with the four predictive controllers used by the PMSG is introduced. The following illustrations present the combined power flow diagrams for the four internal predictive controllers.

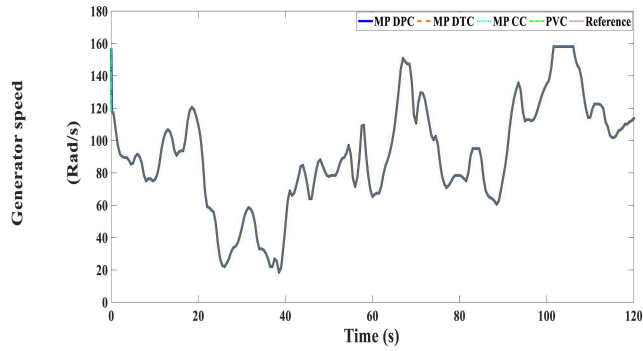


FIGURE 25. Generator speed.

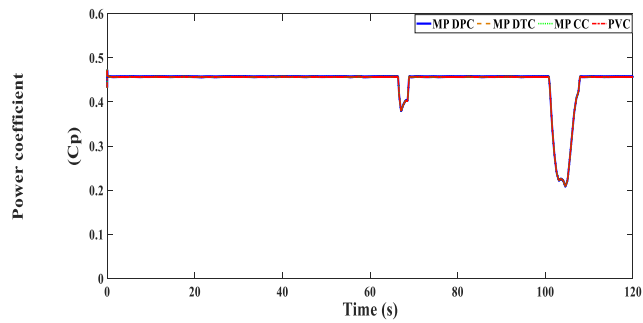


FIGURE 26. Turbine power coefficient.

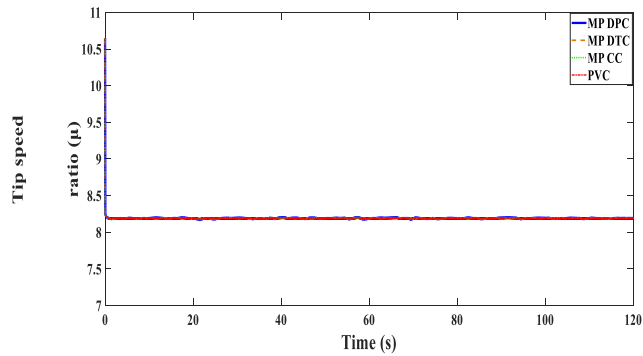


FIGURE 27. Tip speed ratio.

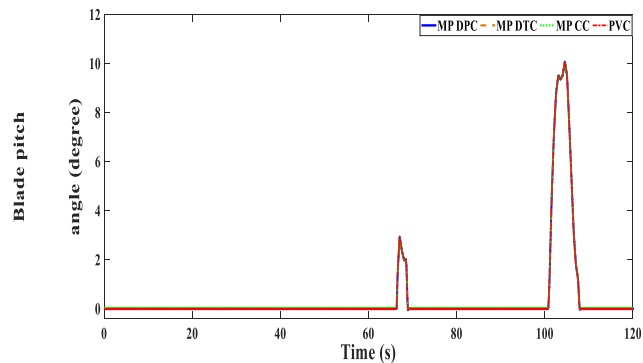


FIGURE 28. Blade pitch angle.

In addition, the operating modes related to each power change are also shown. Figs. 13, 14, 15 and 16 show the combined power flows under the four predictive schemes, while Figs. 17, 18, 19, 20, 21, 22 and 23 show the operating

TABLE 2. Power flow state during different intervals.

Time intervals	Power flow state
1.15→3.6 s, 10→12.2 s, 20.4→23.5 s, 30→33.5 s, 40→43.5 s, 50→53.5 s, 60→63.5 s, 80→83.5 s, 90→91.4 s.	The battery storage system (BSS) compensates the power shortage to ensure operating the pump at its nominal power.
18.9→20 s, 65.6→73.5 s, 73.5→80 s, 86.3→90 s, 92.5→120 s	During these intervals, the excess power is rejected. The HPS during these times is in oversize condition.
3.6→10 s, 13.5→18.9 s, 23.5→30 s, 33.5→40 s, 43.5→50 s, 53.5→60 s, 63.5→65.6 s, 83.5→86.3 s.	During these periods, the generated power is higher than the demand, and the BSS absorbs the surplus power

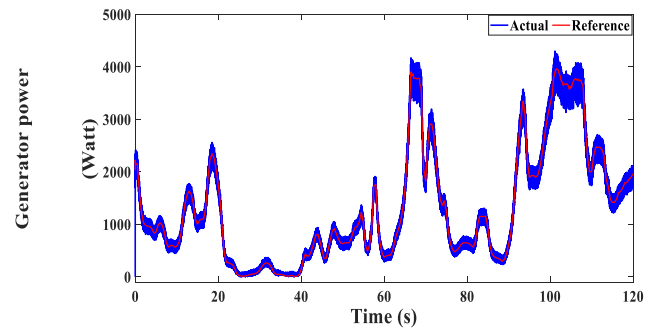


FIGURE 29. PMSG active power under MP DPC.

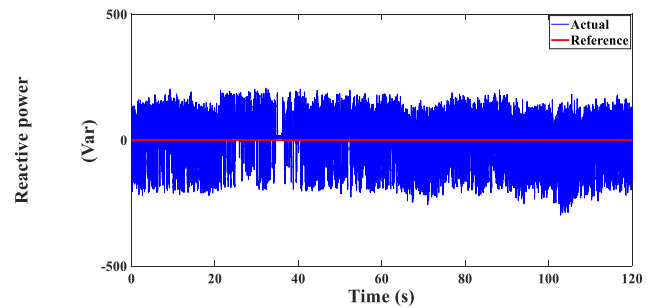


FIGURE 30. PMSG reactive power under MP DPC.

modes. These results are considered as a validation to the designed PMS and the sequence of operation modes described previously in Sec. A.2 and Fig. 3.

In the combined power diagrams, the PMSG power, the battery power, the pump power and the excess power are illustrated. By checking the relevant operating modes figures, it can be realized that at majority of times, the developed PMSG power arecovering the pump power requirements. Meanwhile, power flow during the other time intervals can be summarized as in Table 2.

From the analysis of power flow states and the related operating modes, it can be confirmed that the designed PMS has approved its ability in achieving a balanced power exchange between the different units of the HPS.

Before analyzing the dynamics of the four predictive controllers used for PMSG; the wind speed profile, the generator speed, the turbine power coefficient ( $C_p$ ), the ratio ( $\mu$ ) and



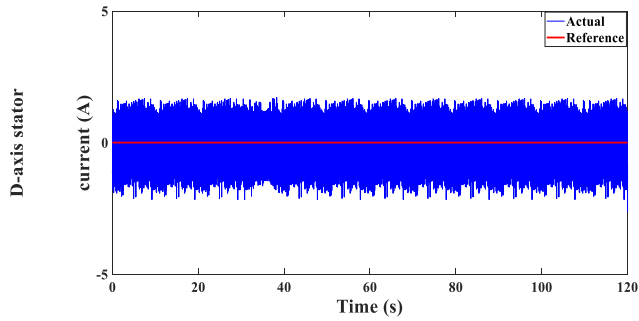


FIGURE 31. D-axis stator current under MP DPC.

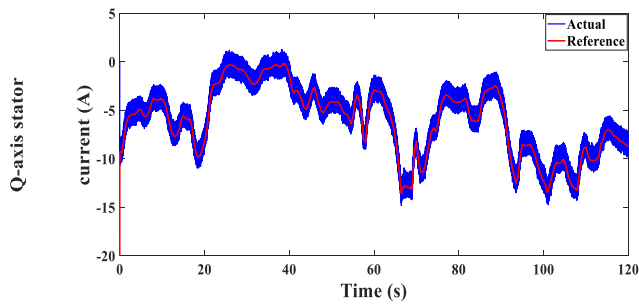


FIGURE 32. Q-axis stator current under MP DPC.

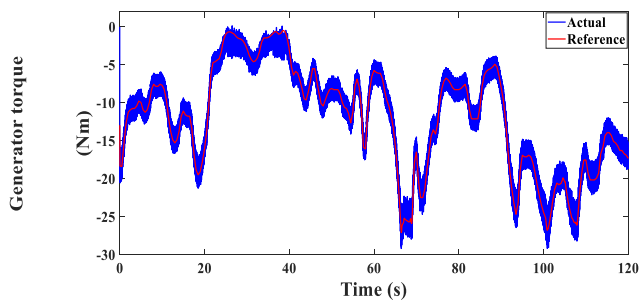


FIGURE 33. PMSG torque under MP DPC.

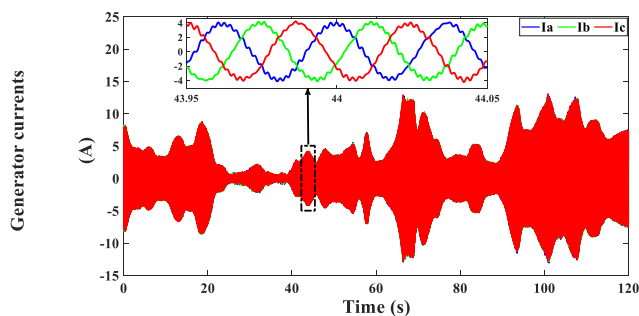


FIGURE 34. PMSG stator currents under MP DPC.

the angle ( $\beta$ ) profiles are primarily presented in Figs. 24, 25, 26, 27 and 28, respectively. These captured behaviors are presented for the four predictive controllers. It is observed that the generator speed is tracking the change in wind speed, also it can be noticed that the tip speed ratio ( $\mu$ ) is maintained to its optimal value in order to achieve optimal power extraction. It can be noticed also that the pitch angle control is activated when the wind speed exceeds its nominal value.

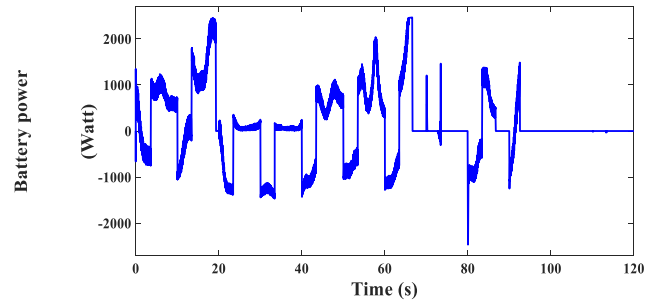


FIGURE 35. Battery power under MP DPC.

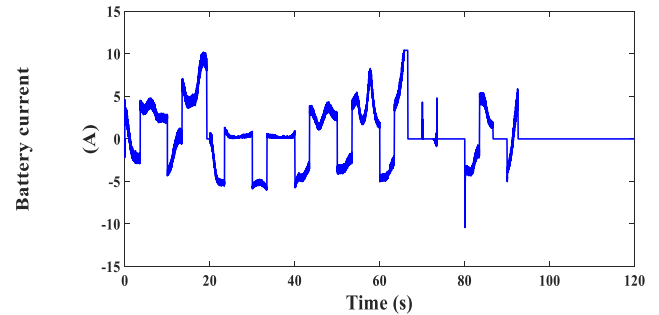


FIGURE 36. Battery current under MP DPC.

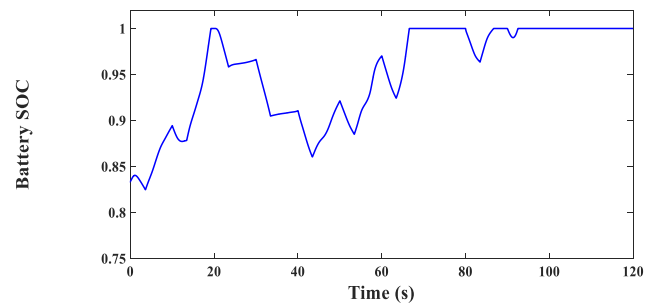


FIGURE 37. Battery SOC under MP DPC.

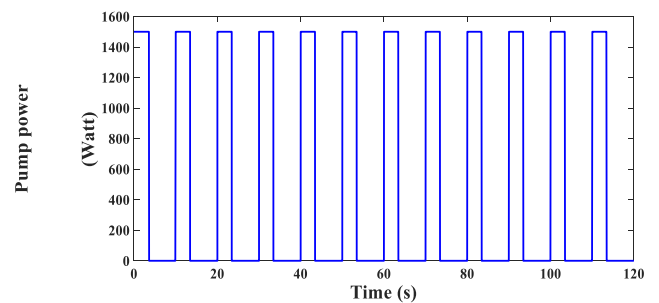


FIGURE 38. Pump demand power under MP DPC.

This is observed from the values of  $C_p$  and  $\beta$  which exhibit a decrease and an increase, respectively in order to restrict the turbine power.

### A. INTERNAL UNITS CONTROL ANALYSIS

#### 1) PERFORMANCE ANALYSIS WITH MP DPC

After analyzing the performance of PMS and the control of wind turbine system; in the current test, the MP DPC control

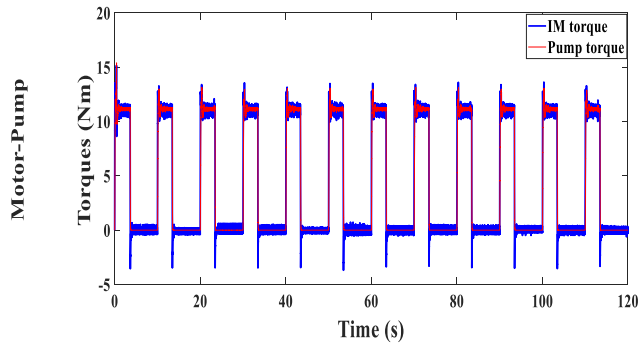


FIGURE 39. Motor-pump torques under MP DPC.

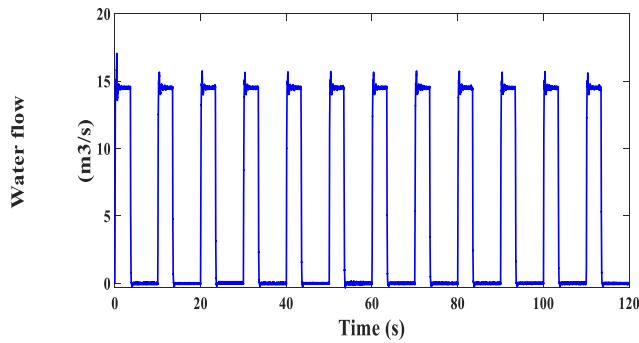


FIGURE 40. Water flow rate under MP DPC.

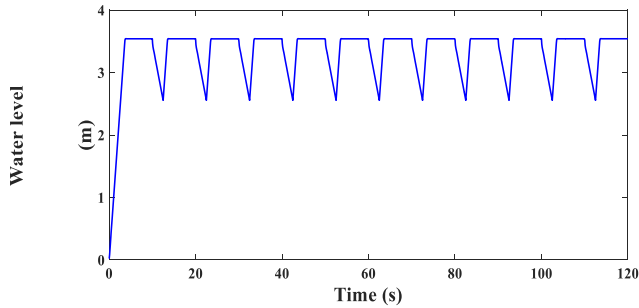


FIGURE 41. Water level under MP DPC.

technique [45] is tested for regulating the generated power from the wind driven PMSG. The validness of the MP DPC technique is approved through ensuring the tracking of actual active and reactive powers,  $d$ - $q$  stator current components and generator torque to their corresponding reference values. This has been presented in Figs. 29, 30, 31, 32 and 33, respectively. The active power tracks the wind speed dynamics, meanwhile the reactive power is kept at zero value. The  $q$ -axis stator current and also the torque are following the change in active power, meanwhile the  $d$ -axis current is held appropriately at zero. However a good tracking is achieved, but the ripples are noticeable in the controlled PMSG variables and in battery power and current as well.

Figure 34 shows the PMSG currents which follows in its dynamic the wind variation. The battery variables; specifically the battery power, battery current and its state of charge (SOC) are illustrated respectively in Figs. 35, 36, and 37.

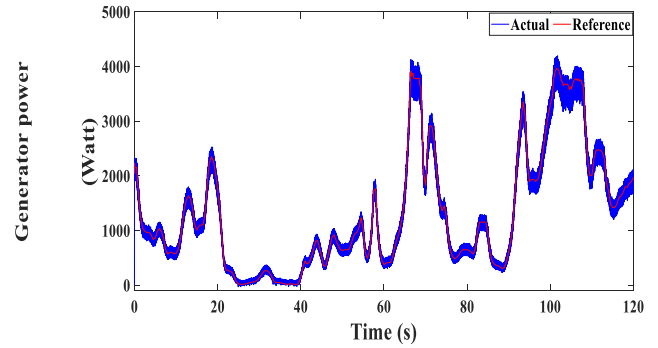


FIGURE 42. PMSG active power under MP DTC.

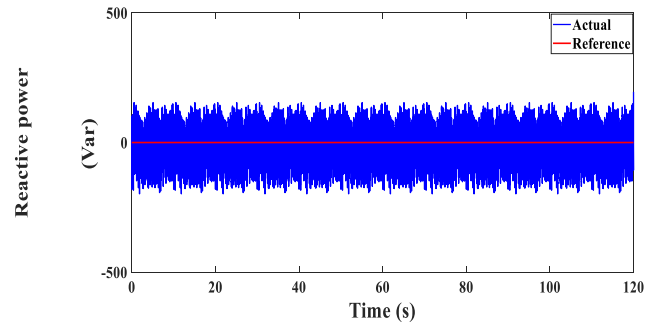


FIGURE 43. PMSG reactive power under MP DTC.

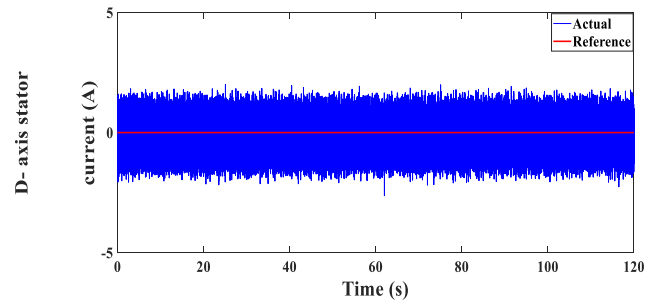


FIGURE 44. D- axis stator current under MP DTC.

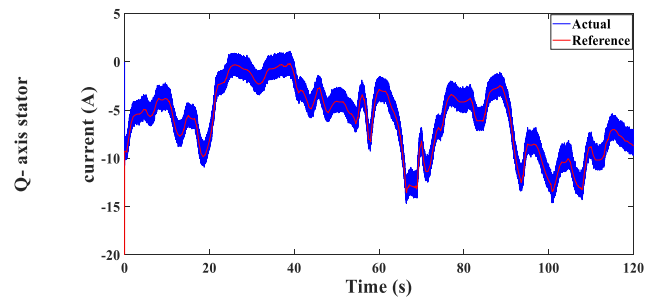


FIGURE 45. Q- axis stator current under MP DTC.

The pump power, the IM motor-pump torques, the water flow and water tank level are also shown in Figs. 38, 39, 40 and 41, respectively. It can be noticed from these figures that each time the water height is reduced below its reference (3.5 m), the PMS activate the power delivery to the pumping system and the pump starts to operate

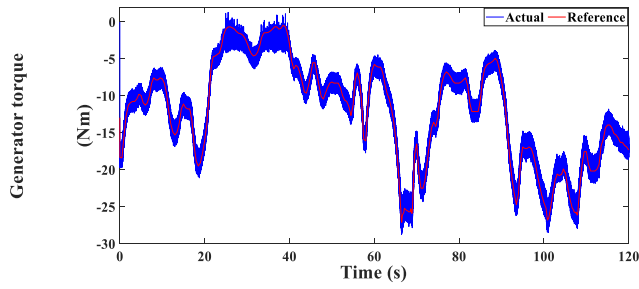


FIGURE 46. PMSG torque under MP DTC.

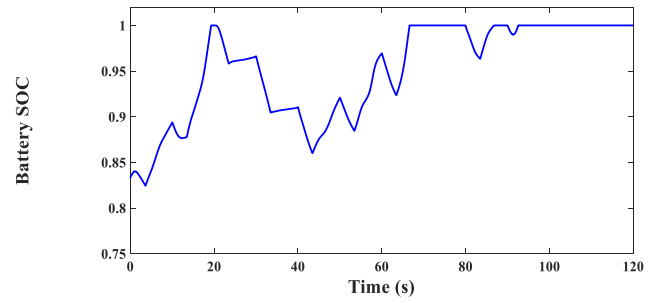


FIGURE 50. Battery SOC under MP DTC.

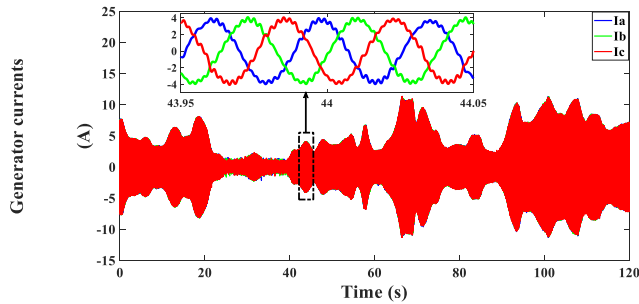


FIGURE 47. PMSG currents under MP DTC.

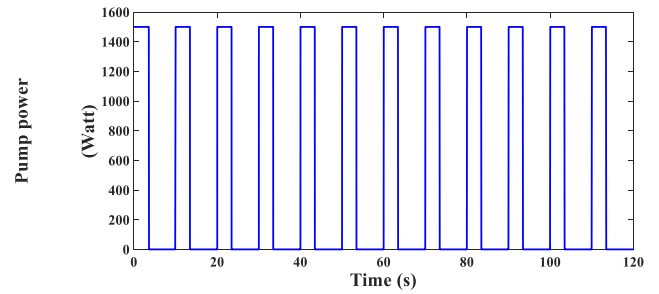


FIGURE 51. Pump demand power under MP DTC.

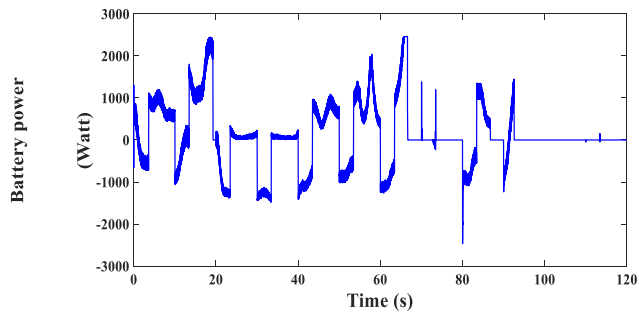


FIGURE 48. Battery power under MP DTC.

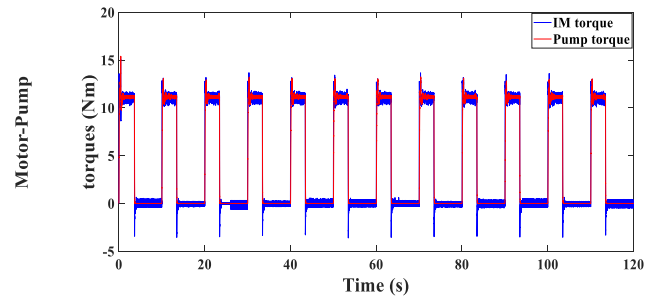


FIGURE 52. Motor-Pump torques under MP DTC.

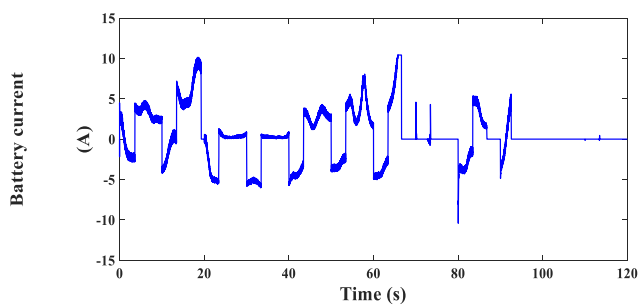


FIGURE 49. Battery current under MP DTC.

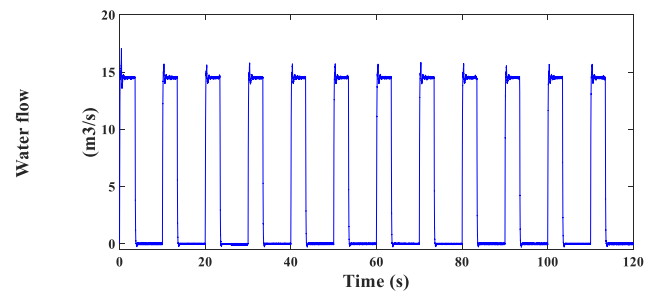


FIGURE 53. Water flow rate under MP DTC.

reciprocally to compensate the water shortage. The IM torque is also properly controlled to balance the pump load on it.

## 2) PERFORMANCE ANALYSIS WITH MP DTC

The wind generation system dynamics are also evaluated utilizing the MP DTC technique [44]. The captured results shown in Figs. 42, 43, 44, 45 and 46 are representing the active and reactive powers, the  $d$ - $q$  stator current components and the PMSG torque, respectively. The MP DTC provides

sufficient behavior through maintaining the actual values concise with their references. However, the accompanied ripples are obvious in the generator quantities. The MP DTC ripples are to some extent lower slightly than that of the MP DTC as it will be revealed in the comparison section.

The generated currents profile is also shown in Fig. 47, which shows that the current variation is emulating the variation in the generated power and in turn emulating the wind speed variation. Figs. 48, 49 and 50 illustrate the battery power, battery current and battery state of charge,

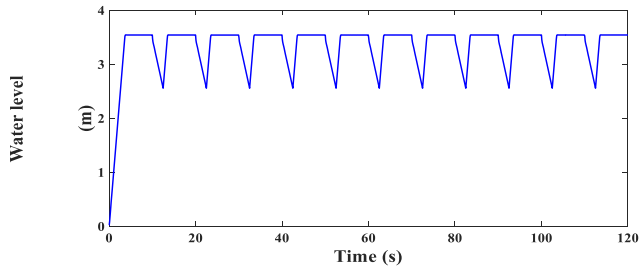


FIGURE 54. Water tank height under MP DTC.

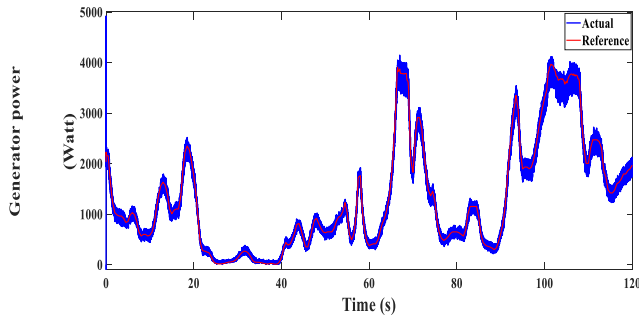


FIGURE 55. PMSG active power under MP CC.

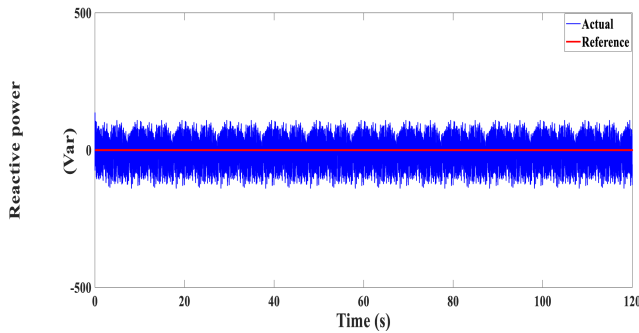


FIGURE 56. PMSG reactive power using MP CC.

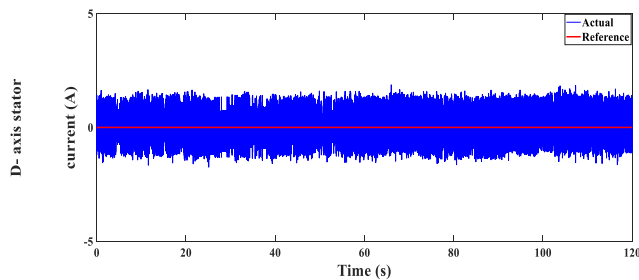


FIGURE 57. D- axis stator current using MP CC.

respectively. Through these figures, it can be shown that the battery dynamics is well managed through adopting the PMS strategy which governs the BSS behavior.

In addition, the validity of the PMS is observed through the obtained dynamics of motor-pump unit. This is illustrated through Figs. 51, 52, 53 and 54 which show the pump power demand, the motor-pump torques, the power flow rate, and the water level inside the tank. From these illustration, it is realized that the PMS enable the pump operation at each

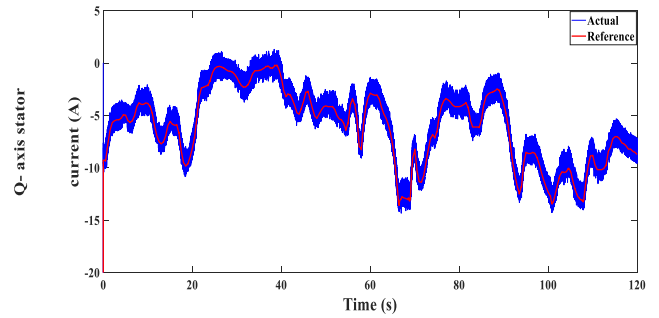


FIGURE 58. Q- axis stator current using MP CC.

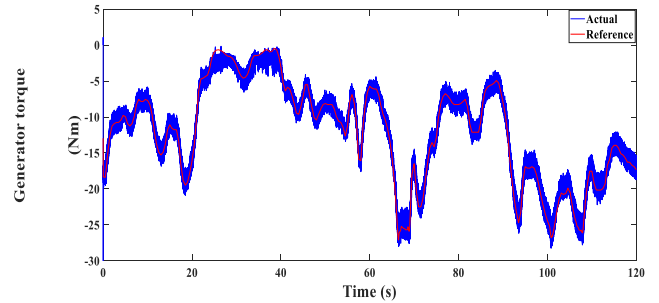


FIGURE 59. PMSG torque using MP CC.

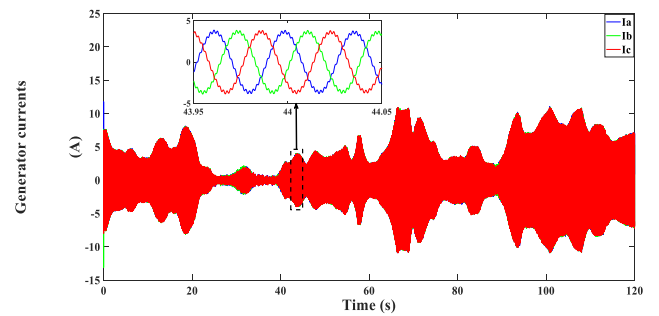


FIGURE 60. PMSG currents using MP CC.

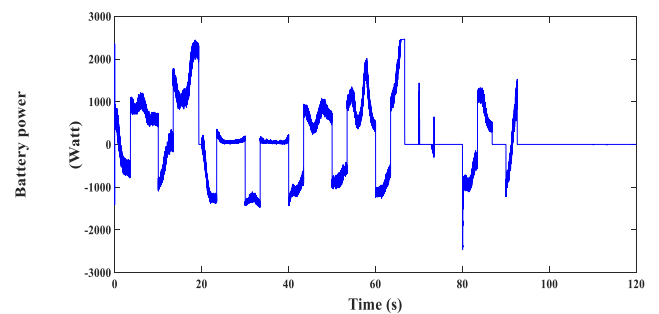


FIGURE 61. Battery power using MP CC.

instant happens that the water level decrease below the reference height (3.5 m); in addition the IM succeeded in tracking the reference torque provided by the PMS according to the pump requirement.

### 3) PERFORMANCE ANALYSIS WITH MP CC

The dynamics of the designed HPS is tested considering the MP CC technique [48] as a controller for the PMSG.

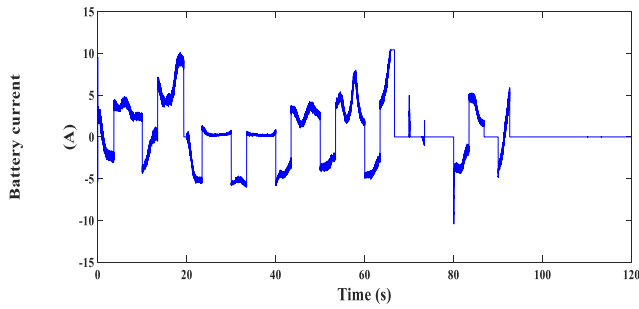


FIGURE 62. Battery current using MP CC.

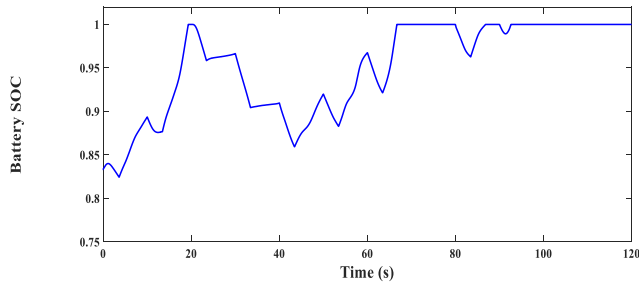


FIGURE 63. Battery SOC using MP CC.

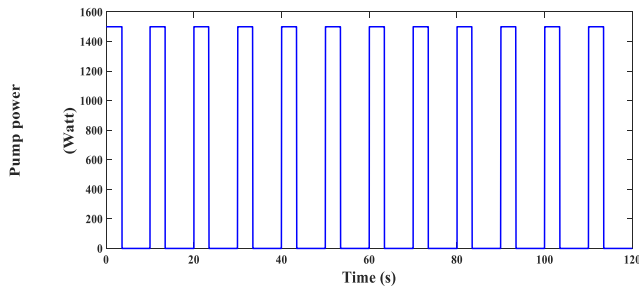


FIGURE 64. Pump demand power using MP CC.

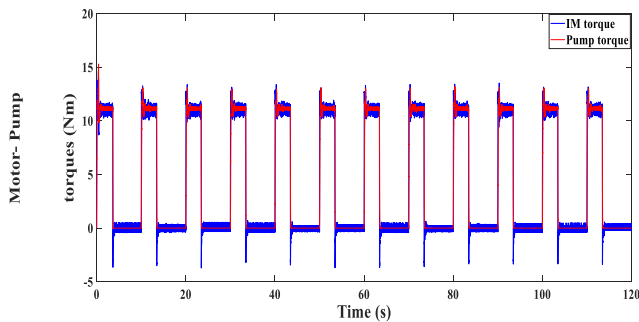


FIGURE 65. Motor-pump torques using MP CC.

The calculated values of active and reactive powers,  $d$ - $q$  generator currents and the generator torque are shown respectively in Figs. 55, 56, 57, 58 and 59. In general, the controlled variables under the MP CC are exhibiting good tracking for their references, however the signal fluctuations are still remarkable. This fact is also noticed in the generated currents profile in Fig. 60. The validity of the BSS system control is also verified in this test; as illustrated in Figs. 61, 62 and 63 which show the battery power, battery current and the

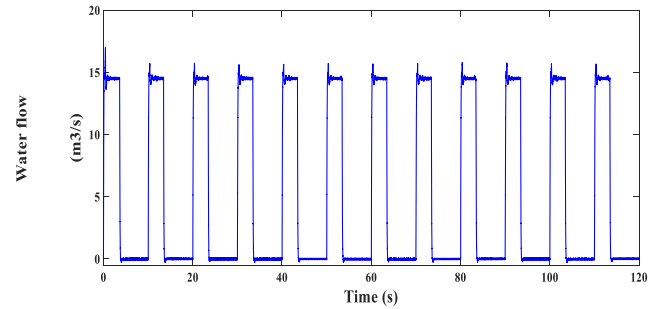


FIGURE 66. Water flow rate using MP CC.

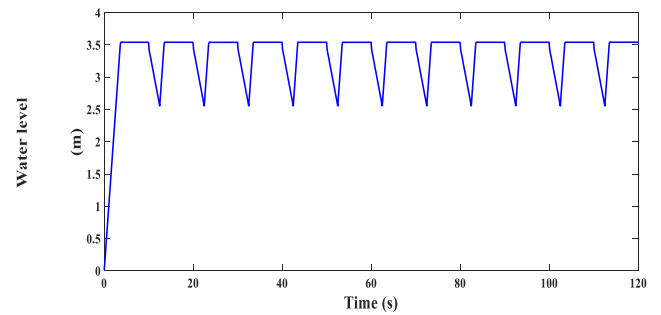


FIGURE 67. Water tank level using MP CC.

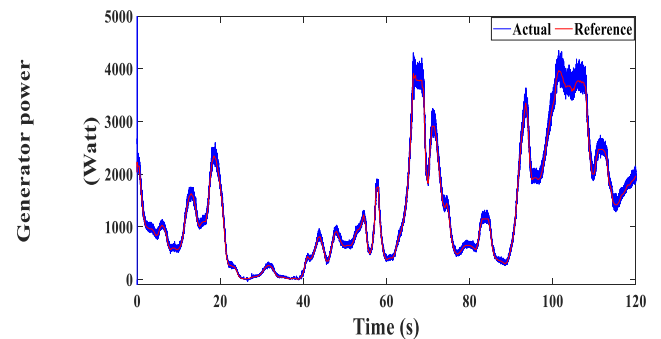


FIGURE 68. PMSG active power with proposed PVC.

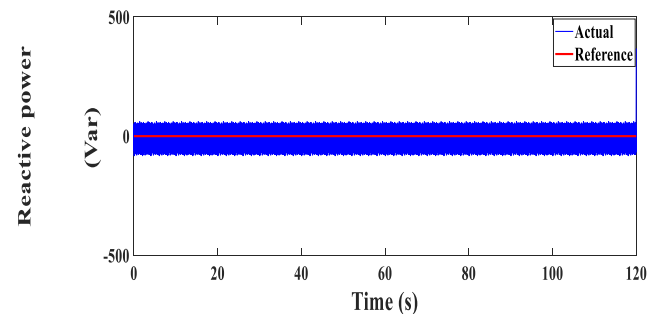


FIGURE 69. PMSG reactive power with proposed PVC.

battery SOC. From these figures, it can be confirmed that the BSS control is effectively achieved. Also, the control performance of pump-motor unit is illustrated in Figs. 64, 65, 66 and 67 which respectively show the pump power, the torques of IM and pump, the water flow rate and the water level inside the tank. It can be noticed that the designed PMS has successfully managed the pumping system at each instant

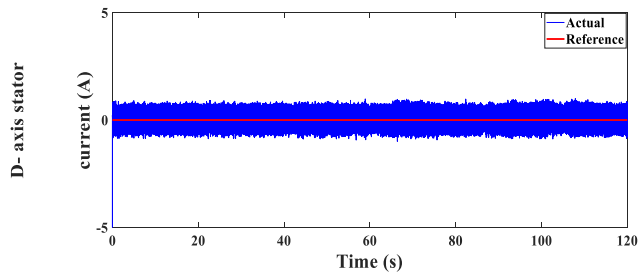


FIGURE 70. D- axis current with proposed PVC.

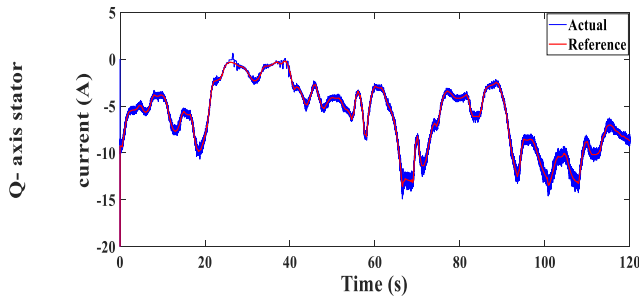


FIGURE 71. Q- axis current with proposed PVC.

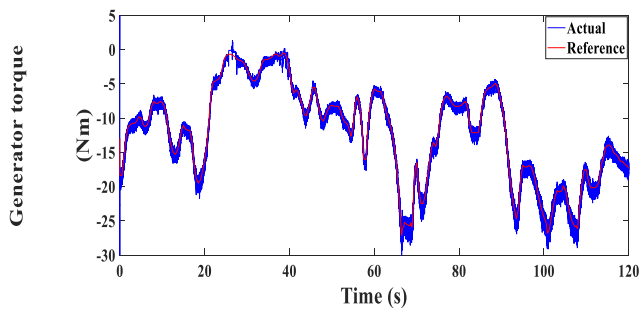


FIGURE 72. PMSG torque with proposed PVC.

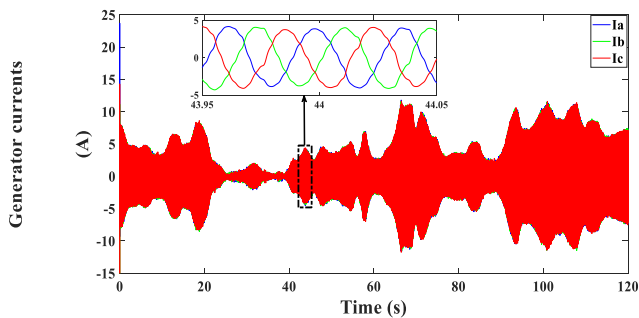


FIGURE 73. PMSG stator currents with proposed PVC.

happens that the water level decreases below the predefined level.

#### 4) PERFORMANCE ANALYSIS WITH PROPOSED PVC

The dynamics of the HPS is also evaluated when considering the proposed PVC to manage the PMSG operation. The obtained results are illustrated in Figs. 68, 69, 70, 71 and 72 which show respectively the active and reactive powers, the  $d$ - $q$  current components and the encounter generator

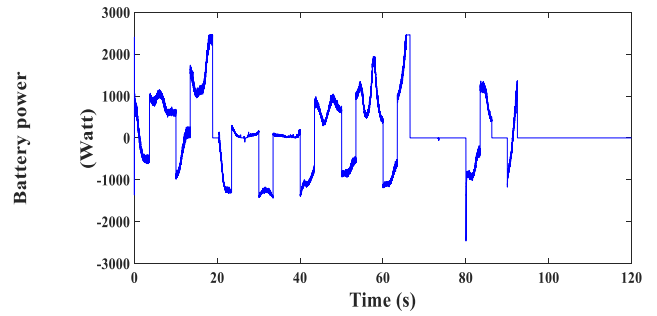


FIGURE 74. Battery power with proposed PVC.

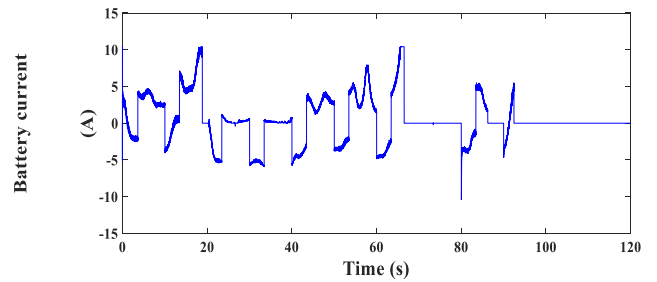


FIGURE 75. Battery current with proposed PVC.

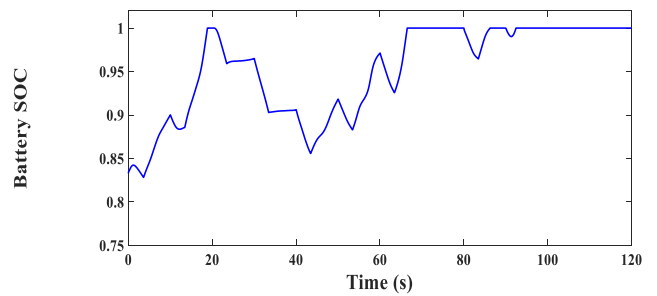


FIGURE 76. Battery SOC with proposed PVC.

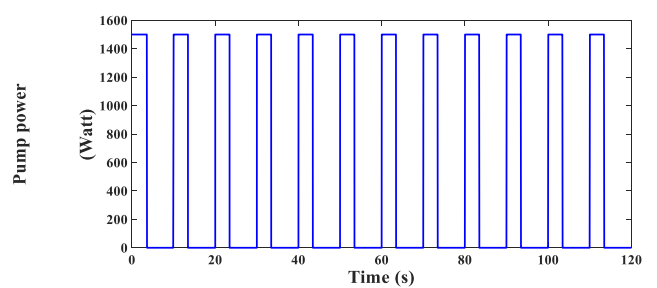


FIGURE 77. Pump demand power with proposed PVC.

torque. By checking these figures and comparing it with their relevant values obtained using the MP DPC and MP DTC, it is obviously realized that the proposed control achieves better dynamics than the other predictive controllers. The ripples content is appropriately limited. The generator currents profile is also shown in Fig. 73, which exhibits less current harmonics in comparison with the current values under MP DPC and MP DTC. This fact is also approved in the captured values of the battery power and current as shown in Figs. 74 and 75. The battery SOC is also presented in Fig. 76. The dynamics

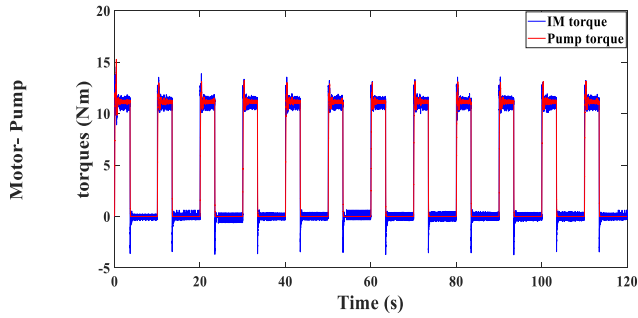


FIGURE 78. Motor-pump torques with proposed PVC.

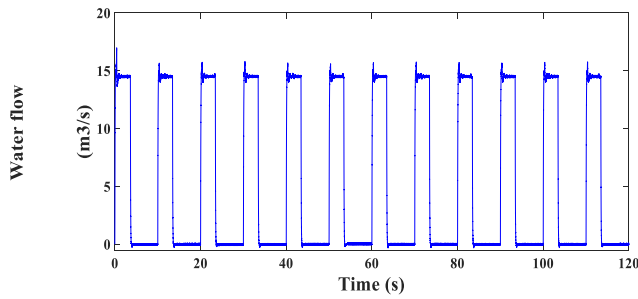


FIGURE 79. Water flow rate with proposed PVC.

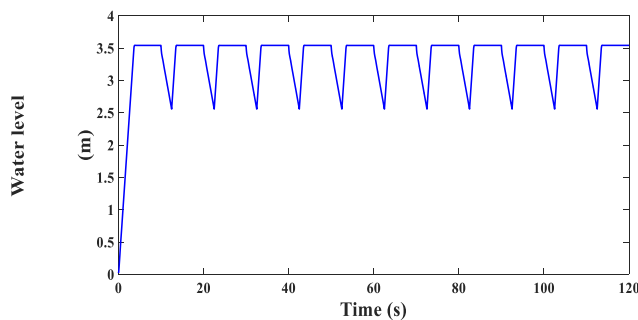


FIGURE 80. Water height with proposed PVC.

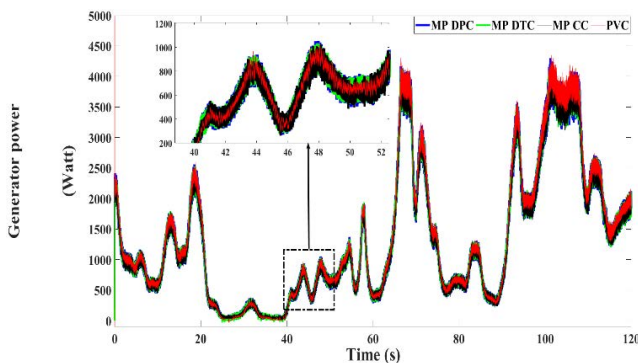


FIGURE 81. PMSG active power with four controllers.

of the motor-pump unit are also presented in Figs. 77, 78, 79 and 80 showing the pump power demand, the motor-pump torques, water flow rate and water height inside the tank. The adaptation of the water level is appropriately achieved thanks to the designed PMS which provides the IM with the optimal reference speed and torque to operate the pump.

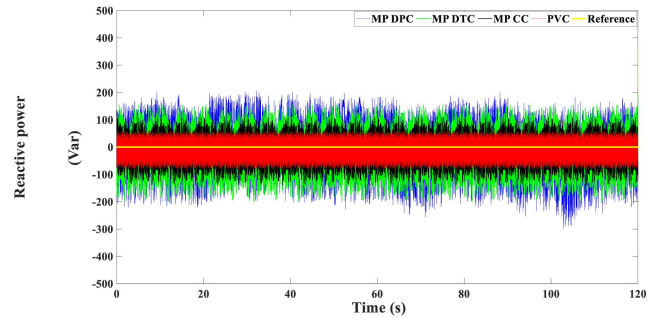


FIGURE 82. PMSG reactive power with four controllers.

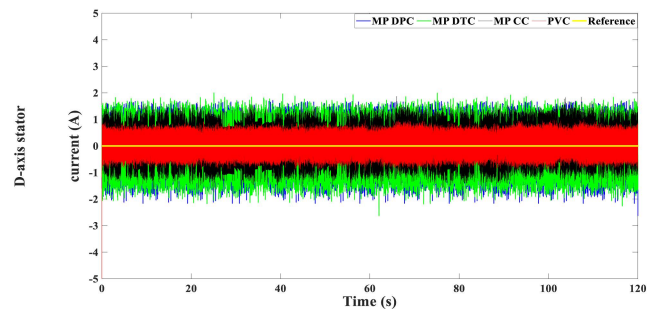


FIGURE 83. D-axis current with four controllers.

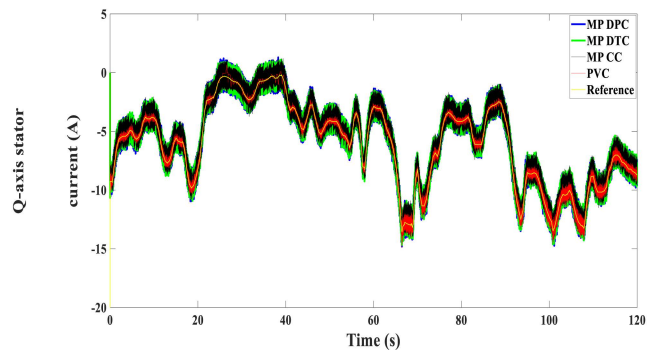


FIGURE 84. Q-axis current with four controllers.

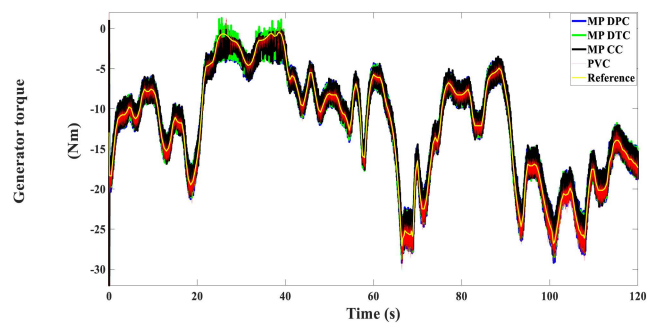


FIGURE 85. PMSG torque with four controllers.

### 5) COMPARATIVE PERFORMANCE ANALYSIS BETWEEN THE FOUR PREDICTIVE CONTROLLERS

After analyzing the performance of each control technique in the previous sections, the current section presents the comparison between the four controllers. From the presented results, it is recognized that the proposed control achieves the

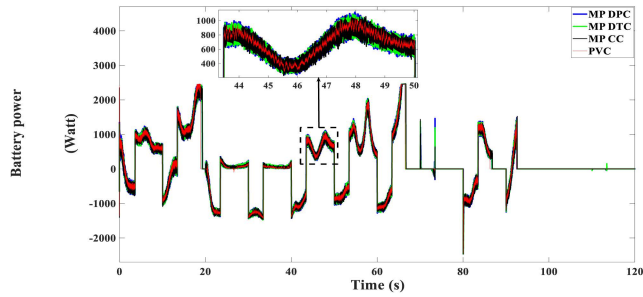


FIGURE 86. Battery power with four controllers.

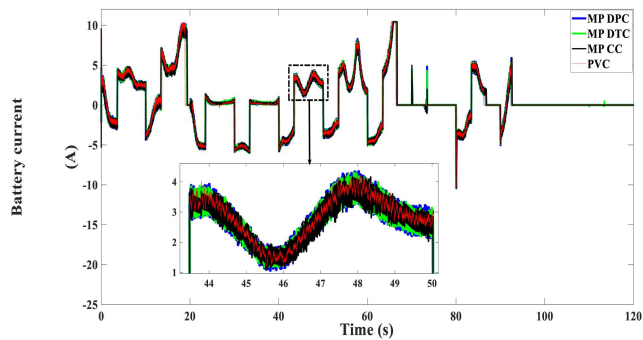


FIGURE 87. Battery current with four controllers.

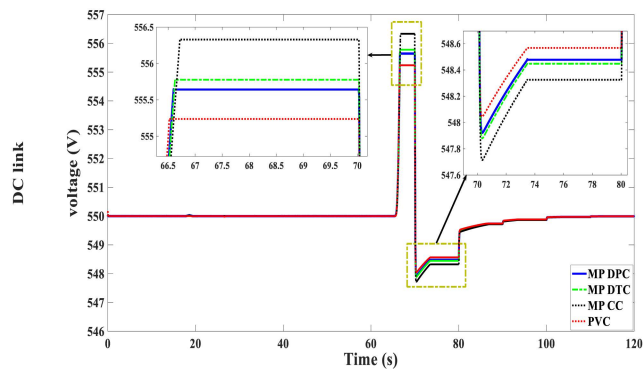


FIGURE 88. DC link voltage with four controllers.

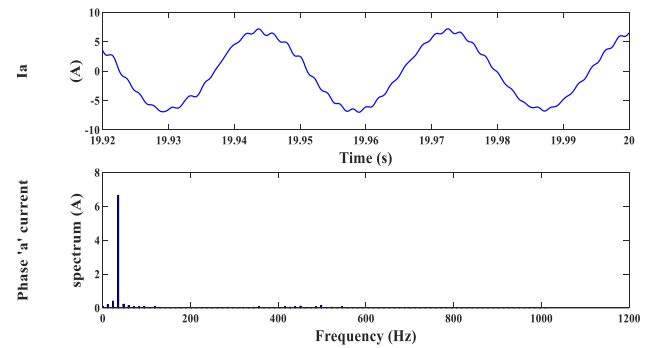
lowest ripples. This is illustrated in Figs. 81, 82, 83, 84 and 85 which present the active and reactive powers, the  $d$ - $q$  axes currents and the generator torque under the three controllers. Meanwhile, Figs. 86 and 87 illustrate the battery power and current for the four controllers, respectively. Moreover, the combined DC link voltage profile is shown in Fig. 88, from which it can be seen that the PVC provides less voltage fluctuation compared with the other three techniques.

The comparison between the four predictive controllers is also applied using the commutation as a measuring tool. This comparison is very vital for any predictive controller, as the predictive control is naturally time consuming. So reducing the computation time and consequently the computation burdens are vital need. Table 3 illustrates the performed commutations under the four controllers.

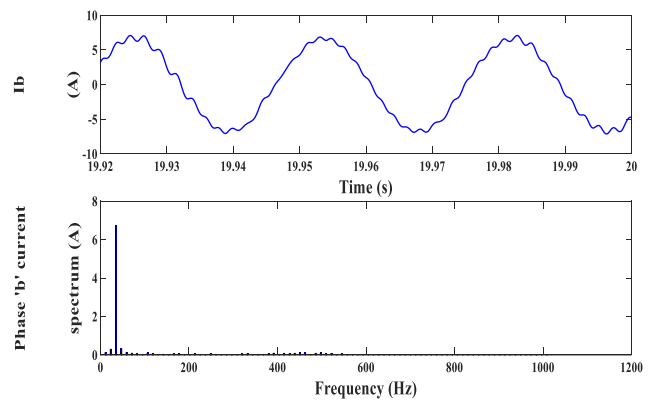
From this comparison, the validness of the proposed predictive control is approved through reducing the number of

TABLE 3. Performed commutation.

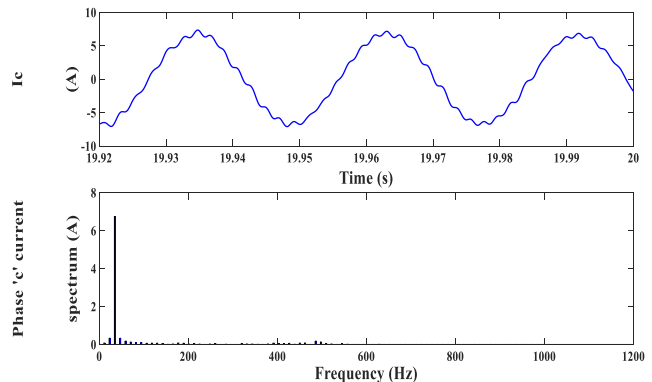
Technique	No of commutations
MP DPC	253600
MP DTC	296100
MP CC	323700
Proposed PVC	70260



(a) Current 'a'



(b) Current 'b'



(c) Current 'c'

FIGURE 89. Current spectrum analysis under MP DPC.

performed commutations which effectively help in limiting the switching losses, and provide a suitable computation environment to be used by the comparable microcontrollers.

An additional analysis for the current harmonics under the four control schemes is also carried out in order to visualize the advantage of the designed control respecting to the other three controllers. The briefed analytical statistics for the currents THD is presented in Table 4. In addition the



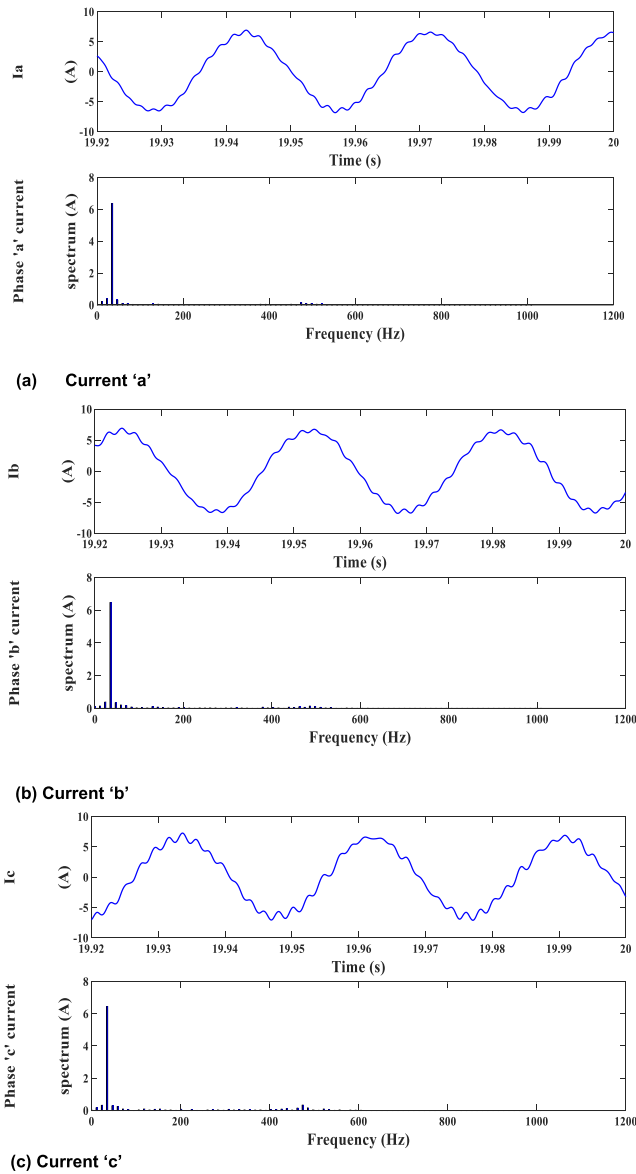


FIGURE 90. Current spectrum analysis under MP DTC.

graphical representation of the currents spectrum are also shown in Figs. 88, 69, 90 and 92 for the the four predictive control systems.

From the figures of current spectrums, it is noticed that the designed control achieves the minimum THD, which helped effectively in improving the quality of the delivered power by the PMSG in comparison with the other predictive controllers used in the literature.

### VII. CONCLUSION

The paper presented a comprehensive dynamic analysis for a renewable energy based water pumping system. The complete system components are constructed and described in details. The power system constituted of a wind turbine, PMSG, a water pumping system (WPS) and a battery storage system (BSS). The BSS is utilized to improve the power

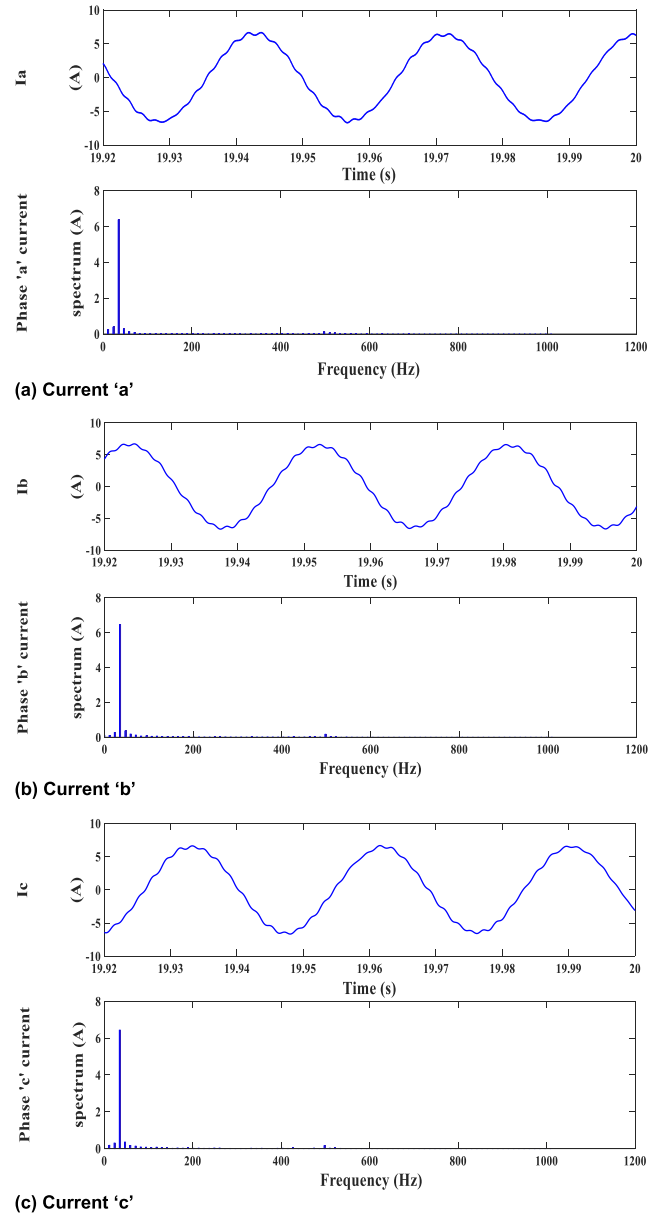


FIGURE 91. Current spectrum analysis under MP CC.

handling to the WPS system under weak wind production. To improve the dynamics of PMSG a new predictive control strategy is formulated which avoids the drawbacks of the traditional predictive control schemes. To confirm the superiority of the designed predictive control technique, extensive evaluation tests are carried out and presented in a comparison form with other three predictive controllers. A power management strategy (PMS) is developed to manage the power flow between the system units to ensure sufficient power delivery to the pumping system. Detailed tests are made to analyze the performance of PMS strategy. The results approved that the proposed PVC has the most effective performance in terms of the reduced ripples, low calculation capacity, structure simplicity and low current THD. The results also approved the validness of the

**TABLE 4. Currents THD analysis.**

Phase	MP DPC	MP DTC	MP CC	Proposed
'a'	Essential (6.65465A) THD (2.54 %)	Essential (6.38869 A) THD (2.06 %)	Essential (6.3842 A) THD (2.01 %)	Essential (6.67833 A) THD (1.46 %)
'b'	Essential (6.72207 A) THD (3.35 %)	Essential (6.48784 A) THD (3.33 %)	Essential (6.48222 A) THD (3.16 %)	Essential (6.75668 A) THD (2.47 %)
'c'	Essential (6.75742 A) THD (3.31 %)	Essential (6.46752 A) THD (3.25 %)	Essential (6.45439 A) THD (3.02 %)	Essential (6.59229 A) THD (2.60 %)

**TABLE 5. PMSG and turbine data.**

Variable	Value	Variable	Value
$r$	2 m	$p$	4
$C_{pmax}$	0.472	$R$	820 mΩ
$\mu_{opt}$	8.1	$L_s$	15.1 mH
$P_{nom}$	3900 W	$\Psi_m$	0.5 Vs
$V_{w,nom}$	10 m/s	$C$	2200 μF
$G$	3.83	$U_{dc}^*$	550 V

**TABLE 6. Parameters of battery.**

Variable	Value	Variable	Value
$R_t$	0.00275 Ω	$L_{bat}$	0.03 H
$R_e$	0.00375 Ω	Capacity	50 Ah
$R_s$	0.00375 Ω	$U_{bat, rated}$	240 V
$C_b$	8837.3 mF	DOD (%)	60 %
$C_s$	82.1 mF	$\eta_{bat}$ %	85 %

designed PMS in balancing the power flow and stabilizing the DC bus voltage as well. Finally, the present study can be used as a base for future work in which additional energy sources (i.e. wave, fuelcell, solar) can be incorporated in favor of studying the system reliability while adopting different types of power management and control algorithms.

**APPENDIX**

**A. DESIGN OF PID CONTROLLER FOR DC BUS CONTROL**

The relationship between the voltage and current of the DC bus can be expressed in the  $s$  domain by

$$\frac{U_{dc}(s)}{I_{dc}(s)} = \frac{1}{sC} \tag{73}$$

The PID operation can be described in the  $s$  domain by

$$H(s) = K_{p,dc} + \frac{K_{i,dc}}{s} + K_{d,dc}s \tag{74}$$

In addition, the relationship between the input DC link voltage error and output reference DC link current

$$U_{dc}(s) - U_{dc}^*(s) * (K_{p,dc}s + K_{i,dc} + K_{d,dc}s^2) = sI_{dc}^*(s) \tag{75}$$

By dividing all sides on  $I_{dc}^*(s)$  and after some manipulations, it results

$$\frac{U_{dc}(s)}{I_{dc}^*(s)} = \frac{(K_{d,dc} + C)s^2 + K_{p,dc}s + K_{i,dc}}{K_{d,dc}Cs^3 + K_{p,dc}Cs^2 + K_{i,dc}Cs} \tag{76}$$

In order to have stable controller dynamics, the characteristic equation of the function (76) must have negative real roots,

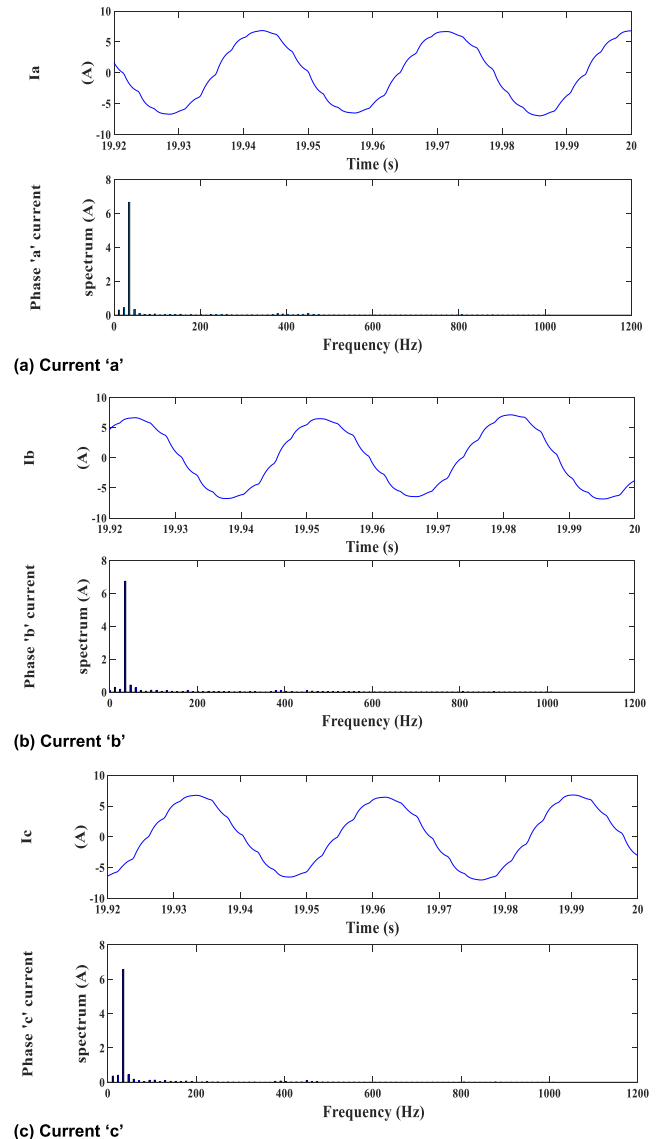


**FIGURE 92. Current spectrum analysis under proposed PFC.**

and this can be achieved via equating the denominator of (76) with zero as follows

$$K_{d,dc}Cs^3 + K_{p,dc}Cs^2 + K_{i,dc}Cs = 0 \tag{77}$$

Alternatively, the open loop (OL) dynamics for a third order system can be represented by the following transfer function [57]

$$H_o(s) = \frac{Y(s+z)}{s^2(s+p)} \tag{78}$$

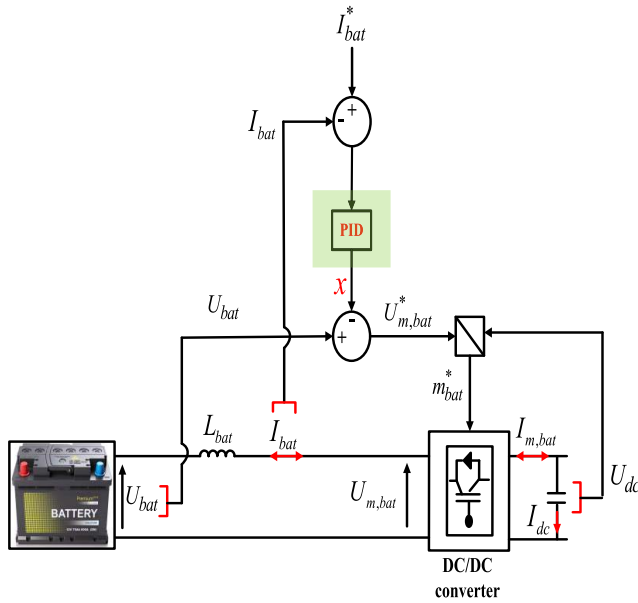


FIGURE 93. BSS control loop.

where  $p$  and  $z$  represent the pole and zero of the OL system, and  $Y$  is the OL gain and it equals the system natural frequency  $\omega_n$ .

Both  $p$  and  $z$  can be defined in terms of the system natural frequency  $\omega_n$  and the damping factor  $\zeta$  as following

$$p = 2\zeta\omega_n \quad \text{and} \quad z = \frac{4\zeta^2}{\omega_n} \quad (79)$$

In a similar to (78), the closed loop (CL) dynamics of a third order system can be described by the following transfer function

$$H_c(s) = \frac{H_o(s)}{1 + H_o(s)} = \frac{\omega_n(s+z)}{s^3 + ps^2 + \omega_n s + \omega_n z} \quad (80)$$

The denominator of (80) represents the characteristic equation which emulates the desired dynamics for a third order system. In order to have a stable operation, the roots of this function must be with negative real values, and accordingly the following condition should be fulfilled

$$s^3 + ps^2 + \omega_n s + \omega_n z = 0 \quad (81)$$

Now, by comparing the relevant terms of (77) and (81), the parameters of PID controller can be determined as following

$$K_{p,dc} = \frac{1}{C}, \quad K_{i,dc} = \frac{2\zeta\omega_n}{C}, \quad K_{d,dc} = \frac{\omega_n}{C} \quad (82)$$

### B. DESIGN OF PID CONTROLLER FOR BSS CONTROL

The PID used for the BSS is illustrated in a section view in Fig. 93, where  $x$  represents the output of the PID controller and it can be expressed in the  $s$  domain by

$$x(s) = U_{bat}(s) - U_{m,bat}^*(s) = U_{bat}(s) - m^*U_{dc}(s) \quad (83)$$

From the voltage balance on the battery terminals, the voltage difference between  $U_{bat}$  and  $U_{m,bat}^*$  represents the

voltage across the inductor  $L_{bat}$  and consequently (83) can be represented assuming zero initial inductor current by

$$x(s) = sL_{bat}I_{bat}(s) \quad (84)$$

Using (84), the input-output dynamic of the PID controller of the BSS can be then expressed by

$$(I_{bat}(s) - I_{bat}^*(s)) * \left( K_{p,B} + \frac{K_{i,B}}{s} + K_{d,B}s \right) = sL_{bat}I_{bat}(s) \quad (85)$$

By dividing all parts of (84) on  $I_{bat}^*(s)$  and by performing some manipulations, the transfer function which governs the dynamics of the designed PID can be expressed by

$$\frac{I_{bat}(s)}{I_{bat}^*(s)} = \frac{K_{d,B}s^2 + K_{p,B}s + K_{i,B}}{(K_{d,B} + L_{bat})s^2 + K_{p,B}s + K_{i,B}} \quad (86)$$

To have stable dynamic operation, the characteristic equation represented by the denominator of (86) should be with negative real roots, consequently the following condition should be fulfilled

$$(K_{d,B} + L_{bat})s^2 + K_{p,B}s + K_{i,B} = 0 \quad (87)$$

On the other hand, the characteristic equation of the second order dynamic system can be defined by

$$s^2 + 2\zeta\omega_n s + \omega_n^2 = 0 \quad (88)$$

Now, by comparing the terms of (87) and (88), the PID parameters are calculated as following

$$K_{p,B} = 2\zeta\omega_n, \quad K_{i,B} = \omega_n^2, \quad K_{d,B} = 1 - L_{bat} \quad (89)$$

### REFERENCES

- [1] V. Telukunta, J. Pradhan, A. Agrawal, M. Singh, and S. G. Srivani, "Protection challenges under bulk penetration of renewable energy resources in power systems: A review," *CSEE J. Power Energy Syst.*, vol. 3, no. 4, pp. 365–379, Dec. 2017.
- [2] Y. Gu, Y. Huang, Q. Wu, C. Li, H. Zhao, and Y. Zhan, "Isolation and protection of the motor-generator pair system for fault ride-through of renewable energy generation systems," *IEEE Access*, vol. 8, pp. 13251–13258, 2020.
- [3] X. Xie, Y. Zhang, K. Meng, Z. Y. Dong, and J. Liu, "Emergency control strategy for power systems with renewables considering a utility-scale energy storage transient," *CSEE J. Power Energy Syst.*, vol. 7, no. 5, pp. 986–995, Sep. 2021.
- [4] M. Motevasel and A. R. Seifi, "Expert energy management of a micro-grid considering wind energy uncertainty," *Energy Convers. Manage.*, vol. 83, pp. 58–72, Jul. 2014.
- [5] C. Abbey, J. Chahwan, and G. Joos, "Energy storage and management in wind turbine," *EPE J.*, vol. 17, no. 4, pp. 6–12, Jan. 2008.
- [6] M. Liserre, T. Sauter, and J. Y. Hung, "Future energy systems: Integrating renewable energy sources into the smart power grid through industrial electronics," *IEEE Ind. Electron. Mag.*, vol. 4, no. 1, pp. 18–37, Mar. 2010.
- [7] H. Mehrjerdi, A. A. M. Aljabery, H. Saboori, and S. Jadid, "Carbon-constrained and cost optimal hybrid wind-based system for sustainable water desalination," *IEEE Access*, vol. 9, pp. 84079–84092, 2021.
- [8] K. Parvin, M. S. H. Lipu, M. A. Hannan, M. A. Abdullah, K. P. Jern, R. A. Begum, M. Mansur, K. M. Muttaqi, T. M. I. Mahlia, and Z. Y. Dong, "Intelligent controllers and optimization algorithms for building energy management towards achieving sustainable development: Challenges and prospects," *IEEE Access*, vol. 9, pp. 41577–41602, 2021.
- [9] G. Pulazza, N. Zhang, C. Kang, and C. A. Nucci, "Transmission planning with battery-based energy storage transportation for power systems with high penetration of renewable energy," *IEEE Trans. Power Syst.*, vol. 36, no. 6, pp. 4928–4940, Nov. 2021.

- [10] O. M. Babatunde, J. L. Munda, and Y. Hamam, "A comprehensive state-of-the-art survey on hybrid renewable energy system operations and planning," *IEEE Access*, vol. 8, pp. 75313–75346, 2020.
- [11] P. Huynh, S. Tungare, and A. Banerjee, "Maximum power point tracking for wind turbine using integrated generator-rectifier systems," *IEEE Trans. Power Electron.*, vol. 36, no. 1, pp. 504–512, Jan. 2021.
- [12] C.-Y. Tang, P.-T. Chen, and J.-H. Jheng, "Bidirectional power flow control and hybrid charging strategies for three-phase PV power and energy storage systems," *IEEE Trans. Power Electron.*, vol. 36, no. 11, pp. 12710–12720, Nov. 2021.
- [13] Y. Tan, K. M. Muttaqi, P. Ciufo, L. Meegahapola, X. Guo, B. Chen, and H. Chen, "Enhanced frequency regulation using multilevel energy storage in remote area power supply systems," *IEEE Trans. Power Syst.*, vol. 34, no. 1, pp. 163–170, Jan. 2019.
- [14] A. Khiareddine, C. Ben Salah, and M. F. Mimouni, "Power management of a photovoltaic/battery pumping system in agricultural experiment station," *Sol. Energy*, vol. 112, pp. 319–338, Feb. 2015.
- [15] O. Alarfaj and K. Bhattacharya, "A controlled load estimator-based energy management system for water pumping systems," *IEEE Trans. Smart Grid*, vol. 9, no. 6, pp. 6307–6317, Nov. 2018.
- [16] A. Joseph and T. R. Chelliah, "A review of power electronic converters for variable speed pumped storage plants: Configurations, operational challenges, and future scopes," *IEEE Trans. Emerg. Sel. Topics Power Electron.*, vol. 6, no. 1, pp. 103–119, Mar. 2018.
- [17] A. Atieh, N. Ahmed, and S. A. Shariff, "Wind speed numerical simulation calculations for novel wind tunnel," in *Proc. IREC 6th Int. Renew. Energy Congr.*, Mar. 2015, pp. 1–4.
- [18] A. Kaabeche and R. Ibtouen, "Techno-economic optimization of hybrid photovoltaic/wind/diesel/battery generation in a stand-alone power system," *Sol. Energy*, vol. 103, pp. 171–182, May 2014.
- [19] A. Hadj Arab, M. Benganem, and F. Chenlo, "Motor-pump system modelization," *Renew. Energy*, vol. 31, no. 7, pp. 905–913, Jun. 2006.
- [20] H. Dagdougui, R. Minciardi, A. Ouammi, and M. Robba, "Modeling and optimization of a hybrid system for the energy supply of a 'Green' building," *Energy Convers. Manage.*, vol. 64, pp. 351–363, Dec. 2012.
- [21] M. Ippolito, M. Silvestre, E. Sanseverino, G. Zizzo, and G. Graditi, "Multi-objective optimized management of electrical energy storage systems in an islanded network with renewable energy sources under different design scenarios," *Energy*, vol. 100, no. 64, pp. 648–662, 2014.
- [22] R. Kallel, G. Boukettaya, and L. Krichen, "Demand side management of household appliances in stand-alone hybrid photovoltaic system," *Renew. Energy*, vol. 81, pp. 123–135, Sep. 2015.
- [23] C. Zioyou, D. Ipsakis, P. Seferlis, S. Bezergianni, S. Papadopoulou, and S. Voutetakis, "Optimal production of renewable hydrogen based on an efficient energy management strategy," *Energy*, vol. 55, pp. 58–67, Jun. 2013.
- [24] W. E. Vanco, F. B. Silva, F. A. S. Goncalves, and C. A. Bissochi, "Evaluation of the capacitor bank design for self-excitation in induction generators," *IEEE Latin Amer. Trans.*, vol. 16, no. 2, pp. 482–488, Feb. 2018.
- [25] K. Teng, Z. Lu, J. Long, Y. Wang, and A. P. Roskilly, "Voltage build-up analysis of self-excited induction generator with multi-timescale reduced-order model," *IEEE Access*, vol. 7, pp. 48003–48012, 2019.
- [26] F. Meng, D. Sun, K. Zhou, J. Wu, F. Zhao, and L. Sun, "A sub-synchronous oscillation suppression strategy for doubly fed wind power generation system," *IEEE Access*, vol. 9, pp. 83482–83498, 2021.
- [27] M. A. Mossa, H. Echeikh, A. A. Z. Diab, and N. V. Quynh, "Effective direct power control for a sensor-less doubly fed induction generator with a losses minimization criterion," *Electronics*, vol. 9, no. 8, p. 1269, Aug. 2020.
- [28] A. M. I. Mohamad, M. Fakhari Moghaddam Arani, and Y. A.-R.-I. Mohamed, "Investigation of impacts of wind source dynamics and stability options in DC power systems with wind energy conversion systems," *IEEE Access*, vol. 8, pp. 18270–18283, 2020.
- [29] M. Kamruzzaman Khan Prince, M. T. Arif, A. Gargoom, A. M. T. Oo, and M. Enamul Haque, "Modeling, parameter measurement, and control of PMSG-based grid-connected wind energy conversion system," *J. Mod. Power Syst. Clean Energy*, vol. 9, no. 5, pp. 1054–1065, 2021.
- [30] L. He, Y. Li, and R. G. Harley, "Adaptive multi-mode power control of a direct-drive PM wind generation system in a microgrid," *IEEE J. Emerg. Sel. Topics Power Electron.*, vol. 1, no. 4, pp. 217–225, Dec. 2013.
- [31] R. Basak, G. Bhuvaneshwari, and R. R. Pillai, "Low-voltage ride-through of a synchronous generator-based variable speed grid-interfaced wind energy conversion system," *IEEE Trans. Ind. Appl.*, vol. 56, no. 1, pp. 752–762, Jan. 2020.
- [32] Z. Zhang, Y. Zhao, W. Qiao, and L. Qu, "A discrete-time direct torque control for direct-drive PMSG-based wind energy conversion systems," *IEEE Trans. Ind. Appl.*, vol. 51, no. 4, pp. 3504–3514, Jul./Aug. 2015.
- [33] Z. Zhang, Y. Zhao, W. Qiao, and L. Qu, "A space-vector-modulated sensorless direct-torque control for direct-drive PMSG wind turbines," *IEEE Trans. Ind. Appl.*, vol. 50, no. 4, pp. 2331–2341, Jul./Aug. 2014.
- [34] P. J. dos Santos Neto, A. Cecilio Pinto, T. A. dos Santos Barros, and E. Ruppert Filho, "A proposal to control active and reactive power in distributed generation systems using small wind turbines," *IEEE Latin Amer. Trans.*, vol. 18, no. 10, pp. 1699–1706, Oct. 2020.
- [35] J. Torres, R. Pena, J. Tapia, J. Riedemann, and C. Pesce, "Direct power control of an axial flux permanent magnet synchronous machine," in *Proc. IEEE Southern Power Electron. Conf. (SPEC)*, Dec. 2017, pp. 1–6.
- [36] A. Harrouz, A. Benatiallah, and O. Harrouz, "Direct power control of a PMSG dedicated to standalone wind energy systems," in *Proc. 8th Int. Conf. Exhib. Ecol. Vehicles Renew. Energies (EVER)*, Mar. 2013, pp. 1–5.
- [37] S. M. Mueyen and A. Al-Durra, "Modeling and control strategies of fuzzy logic controlled inverter system for grid interconnected variable speed wind generator," *IEEE Syst. J.*, vol. 7, no. 4, pp. 817–824, Dec. 2013.
- [38] S. M. Mozayan, M. Saad, H. Vahedi, H. Fortin-Blanchette, and M. Soltani, "Sliding mode control of PMSG wind turbine based on enhanced exponential reaching law," *IEEE Trans. Ind. Electron.*, vol. 63, no. 10, pp. 6148–6159, Oct. 2016.
- [39] L. Bigarelli, M. di Benedetto, A. Lidozzi, L. Solero, S. A. Odhano, and P. Zanchetta, "PWM-based optimal model predictive control for variable speed generating units," *IEEE Trans. Ind. Appl.*, vol. 56, no. 1, pp. 541–550, Jan. 2020.
- [40] H. Wang, J. Yang, Z. Chen, W. Ge, and Y. Ma, "Model predictive control of PMSG-based wind turbines for frequency regulation in an isolated grid," *IEEE Trans. Ind. Appl.*, vol. 54, no. 4, pp. 3077–3089, Aug. 2018.
- [41] A. Linder, R. Kanchan, R. Kennel, and P. Stolze, *Model-Based Predictive Control of Electric Drives*. Göttingen, Germany: Cuvillier Verlag, 2010.
- [42] V. Yaramasu and B. Wu, *Model Predictive Control of Wind Energy Conversion Systems*. Hoboken, NJ, USA: Wiley, 2016.
- [43] Z. Zhang, Z. Li, M. P. Kazmierkowski, J. Rodríguez, and R. Kennel, "Robust predictive control of three-level NPC back-to-back power converter PMSG wind turbine systems with revised predictions," *IEEE Trans. Power Electron.*, vol. 33, no. 11, pp. 9588–9598, Nov. 2018.
- [44] I. Jlassi and A. J. Marques Cardoso, "Enhanced and computationally efficient model predictive flux and power control of PMSG drives for wind turbine applications," *IEEE Trans. Ind. Electron.*, vol. 68, no. 8, pp. 6574–6583, Aug. 2021.
- [45] Z. Zhang, H. Fang, F. Gao, J. Rodríguez, and R. Kennel, "Multiple-vector model predictive power control for grid-tied wind turbine system with enhanced steady-state control performance," *IEEE Trans. Ind. Electron.*, vol. 64, no. 8, pp. 6287–6298, Aug. 2017.
- [46] H. Mahmoudi, M. Aleenejad, P. Moamaei, and R. Ahmadi, "Fuzzy adjustment of weighting factor in model predictive control of permanent magnet synchronous machines using current membership functions," in *Proc. IEEE Power Energy Conf. Illinois (PECI)*, Feb. 2016, pp. 1–5.
- [47] P. R. U. Guazzelli, W. C. de Andrade Pereira, C. M. R. de Oliveira, A. G. de Castro, and M. L. de Aguiar, "Weighting factors optimization of predictive torque control of induction motor by multiobjective genetic algorithm," *IEEE Trans. Power Electron.*, vol. 34, no. 7, pp. 6628–6638, Jul. 2019.
- [48] T. Barisa, S. Iles, D. Sumina, and J. Matusko, "Model predictive direct current control of a permanent magnet synchronous generator based on flexible Lyapunov function considering converter dead time," *IEEE Trans. Ind. Appl.*, vol. 54, no. 3, pp. 2899–2912, May 2018.
- [49] P. Landsmann and R. Kennel, "Saliency-based sensorless predictive torque control with reduced torque ripple," *IEEE Trans. Power Electron.*, vol. 27, no. 10, pp. 4311–4320, Oct. 2012.
- [50] Y. Zhang, W. Xie, Z. Li, and Y. Zhang, "Model predictive direct power control of a PWM rectifier with duty cycle optimization," *IEEE Trans. Power Electron.*, vol. 28, no. 11, pp. 5343–5351, Nov. 2013.
- [51] M. Mossa and Y. Mohamed, "Novel scheme for improving the performance of a wind driven doubly fed induction generator during grid fault," *Wind Eng.*, vol. 36, no. 3, pp. 305–334, 2012.

- [52] A. Vasebi, S. M. T. Bathaee, and M. Partovibakhsh, "Predicting state of charge of lead-acid batteries for hybrid electric vehicles by extended Kalman filter," *Energy Convers. Manage.*, vol. 49, no. 1, pp. 75–82, Jan. 2008.
- [53] R. Jallouli and L. Krichen, "Sizing, techno-economic and generation management analysis of a stand alone photovoltaic power unit including storage devices," *Energy*, vol. 40, no. 1, pp. 196–209, Apr. 2012.
- [54] Z. Shuai, J. Fang, F. Ning, and Z. J. Shen, "Hierarchical structure and bus voltage control of DC microgrid," *Renew. Sustain. Energy Rev.*, vol. 82, pp. 3670–3682, Feb. 2018.
- [55] A. Abdelkafi, A. Masmoudi, and L. Krichen, "Assisted power management of a stand-alone renewable multi-source system," *Energy*, vol. 145, pp. 195–205, Feb. 2018.
- [56] M. A. Mossa, H. Echeikh, and N. V. Quynh, "A novel sensorless predictive voltage control for an induction motor drive based on a back-stepping observer-experimental validation," *IEEE Access*, vol. 9, pp. 11921–11942, 2021.
- [57] H.-M. Wu, H.-G. Yang, T. Yin, and J.-W. Jiao, "Analysis and design of a 3rd order velocity-controlled closed-loop for MEMS vibratory gyroscopes," *Sensors*, vol. 13, no. 9, pp. 12564–12580, Sep. 2013.



**MAHMOUD A. MOSSA** received the bachelor's and master's degrees in electrical engineering from the Faculty of Engineering, Minia University, Egypt, in 2008 and 2013, respectively, and the Ph.D. degree in electrical engineering, in April 2018. Since January 2010, he has been working as an Assistant Lecturer at the Electrical Engineering Department, Minia University. In November 2014, he joined the Electric Drives Laboratory (EDLAB), University of Padova, Italy, for his Ph.D. research activities. Since May 2018, he has been working as an Assistant Professor at the Electrical Engineering Department, Minia University. He is currently a Postdoctoral Fellow at the Department of Industrial Engineering, University of Padova. His research interests include renewable energy systems, power management, optimization, electric machine drives, power electronics, and load frequency control.

**OLFA GAM** received the master's degree from the National Engineering School of Sfax, Tunisia, in 2007, and the Ph.D. degree from the National Engineering School of Monastir, Tunisia, in 2018. Since September 2021, she has been a Research Fellow at the Département École de Genie, Université Québec en Abitibi Témiscamingue, Rouyn-Noranda, QC, Canada. Her research interests include control of grid connected and autonomous isolated plants, optimization of renewable-based systems, energy management of renewable energy-based systems, and power control of PV and wind turbines.



**NICOLA BIANCHI** (Fellow, IEEE) received the M.Sc. and Ph.D. degrees in electrical engineering from the University of Padova, Padova, Italy, in 1991 and 1995, respectively. In 1998, he joined the Department of Electrical Engineering, University of Padova, as an Assistant Professor, where since 2005, he has been an Associate Professor of electrical machines, converters, and drives with the Electric Drive Laboratory, Department of Electrical Engineering. He has authored or coauthored several scientific articles and international books on electrical machines and drives. His research interest includes the field of design of electrical machines, particularly for drive applications. He is a member of the Electric Machines Committee and the Electrical Drives Committee of the IEEE Industry Applications Society. He was a recipient of five awards for best conferences and journal papers. He was a Technical Program Chair of the IEEE Energy Conversion Congress and Exposition in 2014. He is currently an Associate Editor of the IEEE TRANSACTIONS ON INDUSTRY APPLICATIONS.



**NGUYEN VU QUYNH** was born in Vietnam, in 1979. He received the B.S. and M.S. degrees in electrical engineering from the Ho Chi Minh City University of Technology and Education, Vietnam, in 2003 and 2005, respectively, and the Ph.D. degree in electrical engineering from the Southern Taiwan University of Science and Technology, Tainan, Taiwan, in 2013. He is currently the Vice President of Lac Hong University, Dong Nai, Vietnam. His research interests include advanced control techniques, electric machine drives, renewable energy conversion, and robots.

• • •